Scientific Research Publishing

Journal of Applied Mathematics and Physics, 2026, 14(4), 1627-1674
https://www.scirp.org/journal/jamp
ISSN Online: 2327-4379
ISSN Print: 2327-4352

Interference-First Reality: Multi-Observer Emergence of Objectivity and Time from Information Geometry

Michele Bianchi

Independent Researcher, Busto Arsizio, Italy
Email: michele1.bianchi@gsom.polimi.it

How to cite this paper: Bianchi, M. (2026) Interference-First Reality: Multi-Observer Emergence of Objectivity and Time from Information Geometry. *Journal of Applied Mathematics and Physics*, **14**, 1627-1674.
https://doi.org/10.4236/jamp.2026.144077

Received: March 18, 2026
Accepted: April 20, 2026
Published: April 23, 2026

Abstract

We present the Interference-First Reality (IFR) framework, in which physical objectivity is not assumed as primitive but is operationally characterized through the stabilization of observer-induced probability distributions under redundant observation. Within this framework, emergent shared reality is identified with the Fréchet barycenter of an ensemble of observer-induced probability distributions in Jensen-Shannon geometry. A consistency theorem shows that empirical barycenters converge almost surely to their population counterpart as the number of independent observers grows, grounding objectivity in standard metric barycenter theory rather than in additional physical postulates. Alongside this variational construction, we introduce a complementary weighted geometric-overlap estimator and analyze its relation to the barycentric formulation. We instantiate the framework across five physical domains: cosmic microwave background (CMB), heart-rate variability (HRV), JWST spectroscopy, large-scale structure (LSS), and gravitational-wave open data (GWOSC). Across all domains, we find reproducible multi-observer collective summaries, bounded Jensen-Shannon distances consistent with stabilization, and a cross-domain distinguishability hierarchy stable under bootstrap resampling and insensitive to the choice between arithmetic and geometric aggregation. Permutation-based null tests further show that the observed clustering structure exceeds domain-specific random baselines. The empirical scope is nevertheless domain-specific: the GW cross-event comparison mainly reflects observational context and noise geometry, while the JWST case probes structured instrumental heterogeneity within a common observing program rather than independent platforms. Finally, we outline an extension in which time is defined as cumulative informational arc-length between successive stabilized collective states, leaving its full development to a companion study.

Keywords

Interference-First Reality, Information Geometry, Jensen-Shannon Distance, Fréchet Barycenter, Multi-Observer Stabilization, Emergent Objectivity, Probability Simplex, Cross-Domain Inference, CMB, HRV, JWST, LSS, GWOSC

1. Introduction: Holography, Interference, and Information

Modern theoretical physics has offered several indications that space, time, and classical reality may admit emergent, rather than strictly fundamental, descriptions. The holographic principle [1]-[4], first developed in the context of black-hole thermodynamics and later sharpened through gauge/gravity dualities [5], suggests that physical degrees of freedom may be encoded non-locally on lower-dimensional structures. More broadly, a number of foundational approaches have likewise emphasized that observable reality may arise from deeper relational or non-separable structures, rather than from independently given localized objects. Across these lines of thought, a recurring theme is the central role of information in characterizing physical structure beyond object-based pictures.

Quantum theory, despite its extraordinary empirical success, continues to raise conceptual questions concerning non-separability, contextuality, and the emergence of a shared classical description from individual observational records. These issues motivate the search for representation-level frameworks capable of addressing objectivity and collective stability without modifying established dynamical laws.

In previous work [6] [7], we introduced the *interference-first* perspective, according to which physical observables can be modeled as stabilized manifestations of structured interference patterns, rather than as primary fundamental states. The present formulation develops this perspective within an information-geometric setting based on Shannon entropy [8] and the Jensen-Shannon divergence introduced by Lin [9]. Because the Jensen-Shannon distance defines a bounded and symmetric metric geometry on the probability simplex [10], it provides a natural framework for describing multi-observer aggregation as barycentric stabilization in a well-defined metric space. The central claim of this work is that physical objectivity can be operationally identified with the stabilization of observer-induced probability distributions under redundant observation in Jensen-Shannon geometry.

Relation to Quantum Darwinism and decoherence. The redundancy based mechanism underlying the present framework is conceptually related to, but distinct from, Quantum Darwinism [11] and environment-induced superselection [12]. In those programs, objectivity arises from the proliferation of effectively identical records across environmental fragments within a Hilbert-space ontology. The IFR framework, by contrast, operates *entirely at the level of probability rep-*

resentations: no Hilbert space, no quantum state, and no specific decoherence mechanism is presupposed. Objectivity is instead identified with a geometric invariant—the Fréchet barycenter in the Jensen-Shannon metric on the probability simplex. The relation to Quantum Darwinism is therefore structural and interpretive rather than derivational: IFR supplies an information-geometric layer of description that may be compatible with Hilbert-space accounts, but does not depend on them.

Scope and contributions. Initial empirical analyses of CMB and HRV data, carried out with bounded information-geometric measures, revealed robust coherence structures across distinct physical domains [6] [7]. The present work consolidates and extends this program along three main directions.

1) **Theoretical consolidation.** We formalize the multi-observer framework in which objectivity is identified with the stabilization of empirical Fréchet means in the Jensen-Shannon metric, and we provide a complete proof of the barycenter consistency theorem (Theorem 1) supporting this identification.

2) **Empirical extension.** We extend the framework to gravitational-wave open data (GWOSC) and JWST spectroscopy, and broaden the LSS analysis to both redshift-space $p(z)$ and Fourier-space $p(k)$ representations, thereby testing the framework across distinct observational layers and assumption regimes.

3) **Null-test validation.** For each domain, we construct permutation-based null distributions to verify that the observed barycentric clustering is not a trivial consequence of normalization or finite-support effects, and to distinguish the reported geometry from generic features of arbitrary normalized distributions.

The present construction introduces neither new dynamical laws nor hidden variables, and it does not modify standard quantum mechanics. It operates entirely at the level of observer-induced probability representations and their associated information-geometric structure. Accordingly, all statements regarding reality, objectivity, and stabilization are formulated in *operational and geometric terms*: they concern collective representational invariants in probability space, rather than ontological claims about microscopic constituents. An extension in which time is defined as cumulative informational arc-length between successive stabilized collective states is outlined only programmatically here and is deferred to a companion study.

2. Formal Framework: Interference Substrate, Projection, and Emergent Geometry

2.1. Interference Substrate (Interference-First Framework)

We begin from a deliberately minimal ontology in which neither spacetime, nor observables, nor a privileged observer is assumed at the foundational level. The primitive entity is an *interference substrate* whose internal degrees of freedom are not interpreted as physical observables in isolation.

Definition 1 (Interference substrate). Let $\{\psi_i\}_{i\in\mathcal{I}}$ be a finite or countable family of complex-valued components defined on a common domain Σ. The interference substrate is defined by

$$\Phi(x) := \mathcal{C}\left(\{\psi_i(x)\}_{i\in\mathcal{I}}\right), \tag{1}$$

where $\mathcal{C}$ denotes a compositional rule acting on the family of components. In the present implementation, the compositional rule is chosen to be multiplicative,

$$\mathcal{C}\left(\{\psi_i(x)\}_{i\in\mathcal{I}}\right) := \prod_{i\in\mathcal{I}} \psi_i(x). \tag{2}$$

No physical observable is assigned to the individual components ψ_i.

This construction encodes the principle that physically relevant structure arises only through mutual interference within the substrate rather than from isolated components.

Remark (Interpretation of the interference substrate). Equation (1) introduces the interference substrate through a generic compositional rule acting on the family of components $\{\psi_i\}$. In the present implementation this rule is chosen to be multiplicative (Equation (2)), but the empirical analyses developed in this work do not depend on the specific form of this composition.

In conventional wave physics, interference typically arises from the superposition (sum) of amplitudes. The multiplicative realization adopted here should therefore not be interpreted as a physical superposition law for wavefields. Instead, it provides a convenient factorized representation of multiple generative constraints acting on the substrate.

Such factorized structures are common in statistical physics and information theory, where joint configurations are naturally expressed as products of independent factors (for example Boltzmann weights or likelihood terms). After projection through the observer map $\Pi(\Phi)$ the framework yields normalized probability distributions on the simplex, where the information-geometric analysis is carried out.

The multiplicative form therefore serves only as a minimal generative representation of the substrate. Alternative compositional rules would lead to the same observable probability geometry after normalization. In this sense the substrate constitutes a minimal ontological commitment of the framework rather than a falsifiable microscopic physical model.

2.2. Observers as Projection Maps and the Probability Simplex

Observable statistics arise only after an observer-dependent projection followed by a normalization that produces a probability state.

Definition 2 (Observer projection). Let $\mathcal{H}$ be a complex separable vector space (e.g. a Hilbert space, though not required) that supports substrate states $\Phi \in \mathcal{H}$. An observer O is modeled as a bounded linear map

$$\Pi_O : \mathcal{H} \to L^2(\Xi_O), \tag{3}$$

where Ξ_O is the observer's representational domain (frequency grid, redshift grid, line-index grid, k-grid, etc.).

Definition 3 (Born—interference probability map). Given $\Phi \in \mathcal{H}$ and an observer O with projection Π_O, define

$$p_O(\xi) = \frac{\left|\Pi_O(\Phi)(\xi)\right|^2}{\int_{\Xi_O} \left|\Pi_O(\Phi)(\xi)\right|^2 \mathrm{d}\xi}, \quad p_O \in \Delta^{\circ}(\Xi_O), \tag{4}$$

where $\Delta^{\circ}(\Xi_O)$ denotes the interior of the probability simplex over Ξ_O.

When the observer projection is implemented by a spectral transform (e.g. Fourier), Equation (4) reduces to

$$p(\xi) = \frac{\left|\mathcal{F}[\Phi](\xi)\right|^2}{\int \left|\mathcal{F}[\Phi](\xi)\right|^2 \mathrm{d}\xi}, \quad p \in \Delta^{\circ}. \tag{5}$$

Note. In the discrete case, $\Xi_O = \{\xi_k\}_{k=1}^{K}$ and Δ° is the open simplex $\left\{p \in \mathbb{R}^K : p_k > 0, \sum_{k=1}^{K} p_k = 1\right\}$. In all computations each observer state satisfies

$$p_i(x_k) \geq 0, \quad \sum_{k=1}^{K} p_i(x_k) = 1, \tag{6}$$

after projection to a common master grid.

2.3. Jensen-Shannon Geometry (Bounded, Symmetric, Multi-Observer Stable)

To quantify distinguishability between observer-induced states we use the Jensen-Shannon (JS) divergence and its induced metric:

$$D_{\mathrm{JS}}(p \,\|\, q) = \frac{1}{2} D_{\mathrm{KL}}(p \,\|\, m) + \frac{1}{2} D_{\mathrm{KL}}(q \,\|\, m), \quad m = \frac{1}{2}(p+q), \tag{7}$$

$$d_{\mathrm{JS}}(p,q) = \sqrt{D_{\mathrm{JS}}(p \,\|\, q)}. \tag{8}$$

The Jensen-Shannon geometry can be viewed as a particular realization of information-geometric structure on the probability simplex [10]. While the present framework does not rely on a specific dual-affine connection, it inherits the geometric viewpoint that probability distributions form a curved statistical manifold. The key operative advantages of d_{JS} over the KL divergence are: 1) *symmetry*; 2) *boundedness* ($d_{\mathrm{JS}} \in \left[0, \sqrt{\ln 2}\right]$ in nats, or $[0,1]$ in bits); and 3) *metric validity* (triangle inequality). Boundedness is crucial for multi-observer aggregation: localized spectral features (narrow-band peaks) that would cause KL to diverge are handled stably by d_{JS}.

2.4. Emergent Reality as an Information-Geometric Barycenter

No observer is privileged. Operationally, the *shared collective state* is defined as the distribution that minimizes total disagreement with the observer ensemble in the JS geometry.

Given $\{p_i\}_{i=1}^{N} \subset \Delta^{\circ}$ and weights $w_i \geq 0$, $\sum_i w_i = 1$, define the exact empirical Fréchet minimizer

$$p^{\mathrm{F}} = \arg\min_{p\in\Delta^{\circ}} \sum_{i=1}^{N} w_i D_{\mathrm{JS}}\left(p_i \parallel p\right). \tag{9}$$

As an interference-first closed-form candidate emphasizing constructive overlap, we also use the weighted geometric overlap estimator

$$p^{\mathrm{G}}\left(x_k\right) = \frac{\prod_{i=1}^{N} p_i\left(x_k\right)^{w_i}}{\sum_{j=1}^{K}\prod_{i=1}^{N} p_i\left(x_j\right)^{w_i}}. \tag{10}$$

This construction corresponds to a Fréchet mean in a metric space [13], with general existence and stability properties established by Sturm [14].

As a linear baseline, we also define the weighted arithmetic mean

$$\bar{p}\left(x_k\right) = \sum_{i=1}^{N} w_i p_i\left(x_k\right). \tag{11}$$

Note. Equation (9) defines the collective state variationally through the exact empirical Fréchet minimizer p^{F}. Equation (10) defines instead a closed-form geometric overlap estimator p^{G}, which is not claimed to coincide with p^{F} in full generality. Its role is practical and interpretive: 1) it is closed-form; 2) it is overlap-selective, suppressing bins where any observer assigns low mass; and 3) it is empirically stable across all domains tested here. Whenever empirical sections report distances to the geometric collective state, the symbol p^{G} is used explicitly.

2.5. Stabilization and the Emergence of Objectivity

Objectivity is interpreted operationally as contraction of dispersion and barycenter stabilization as N increases under redundant, independent observation. This constitutes an information-geometric realization of redundancy based objectivity [11], without presupposing an underlying Hilbert-space ontology.

Define the JS dispersion of an observer set $\left\{p_i\right\}_{i=1}^{N}$ around a candidate center p:

$$\mathcal{V}_N\left(p\right) := \sum_{i=1}^{N} w_i D_{\mathrm{JS}}\left(p_i \parallel p\right). \tag{12}$$

Let $p^{(N)}$ denote any minimizer of $\mathcal{V}_N$.

Theorem 1. (Multi-observer stabilization in Jensen-Shannon geometry) Let $\left\{P_i\right\}_{i\geq 1}$ be independent, identically distributed random probability distributions in the interior of the simplex $\Delta^{\circ} \subset \mathbb{R}^K$, equipped with the Jensen-Shannon metric d_{JS}. Assume:

1) a common representational space (shared master grid);

2) non-vanishing overlap of support (interior-simplex condition);

3) finite second moment with respect to d_{JS}.

Let $p^{(N)}$ denote any empirical Fréchet mean minimizing

$$\mathcal{V}_N\left(p\right) = \sum_{i=1}^{N} w_i D_{\mathrm{JS}}\left(P_i \parallel p\right), \quad \sum_{i=1}^{N} w_i = 1.$$

Then:

a) A population Fréchet mean p^{∞} exists.

b) The empirical barycenters $p^{(N)}$ converge almost surely to the set of population minimizers.

c) If the population minimizer is unique,

$$d_{\mathrm{JS}}\left(p^{(N)},p^{\infty}\right)\xrightarrow[N\to\infty]{a.s.}.$$

Accordingly, in the large-N regime the collective barycenter becomes a stable geometric invariant of the observer ensemble in $\left(\Delta^{\circ},d_{\mathrm{JS}}\right)$.

Proof. See **Appendix A**.

Remark (Interpretation and empirical applicability). Theorem 1 is a standard consistency result for empirical Fréchet means in a bounded metric space, following the metric barycenter theory of [13] [14]. Its role in the present framework is to establish a reference case in which multi-observer barycenters are guaranteed to stabilize as the number of observers increases. The theorem is formulated under the classical assumption that the observer-induced distributions $\{P_i\}$ are independent and identically distributed samples from a common probability measure on the simplex. In the empirical datasets analyzed here, however, the observers are not strictly i.i.d. They correspond instead to heterogeneous but redundant measurement channels (e.g. different gravitational-wave detectors, instrumental modes, sky partitions, or temporal epochs), which may differ in calibration, noise floor, or sampling properties. The role of Theorem 1 is therefore not to assert that these empirical ensembles satisfy the i.i.d. assumption exactly, but to provide the mathematical limit in which stabilization must occur. The empirical analyses in Sections 3-7 test whether similar stabilization behaviour emerges under realistic heterogeneous observation. In this interpretation, the framework requires *redundancy of informational constraints* rather than strict statistical independence: when multiple observers encode overlapping aspects of the same underlying structure, their Jensen-Shannon barycenter remains a well-defined and stable collective representation even in the presence of heterogeneous observation channels.

Checklist for the empirical domains. Theorem 1 is used as a reference case consistency result. Its assumptions map to the empirical domains as follows.

- **Common representational space:** satisfied explicitly in all domains through a shared master grid (frequency, multipole, wavelength, redshift, or *k*-space) before JS comparison.
- **Non-vanishing overlap of support:** satisfied exactly after normalization and common-grid projection in all reported computations; where sparse or sign-sensitive structures arise, the representation is regularized or recoded before distance evaluation.
- **Finite second moment in d_{JS}:** satisfied automatically in practice because the Jensen-Shannon metric is bounded on the simplex.
- **i.i.d. sampling:** best viewed as a limiting idealization rather than an exact empirical condition. It is most closely approximated in repeated or closely aligned observer families (e.g. CMB smoothing configurations, HRV temporal epochs,

redundant LSS partitions), and most clearly relaxed in structured heterogeneous settings such as GW detector networks, JWST instrumental modes, and cross-event GW comparisons.

- **Interpretive role of the theorem:** the empirical sections therefore test stabilization under redundant but heterogeneous observation, not a literal verification of the full i.i.d. theorem in each dataset (Figure 1).

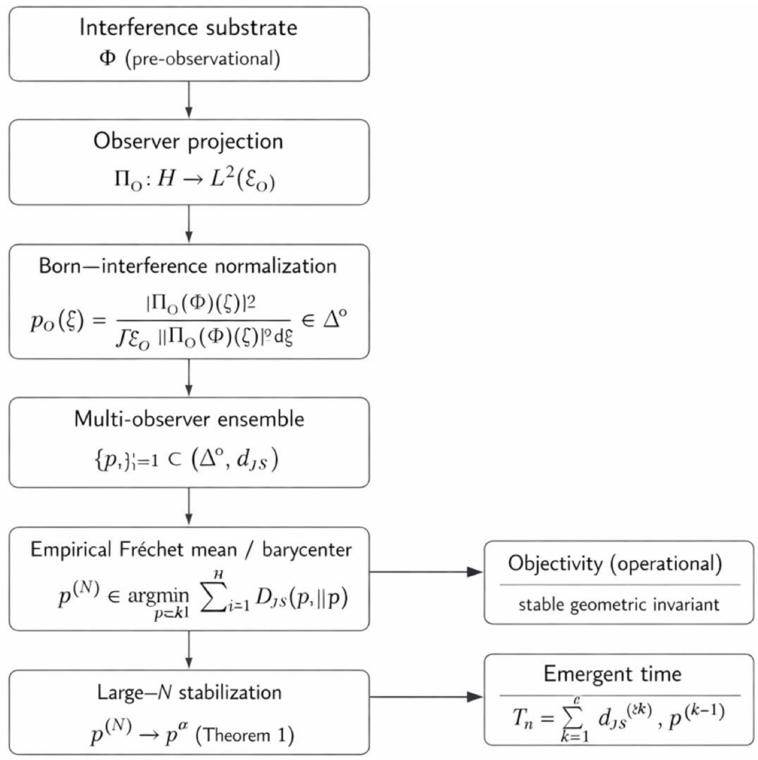

Figure 1. Interference-first multi-observer scheme. Projections of Φ into Δ° are compared via the Jensen-Shannon metric and aggregated by a Fréchet barycenter. Stabilization yields objectivity; cumulative displacement defines emergent time.

2.6. Geometric Interpretation: Stabilization as Multi-Observer Decoherence

The stabilization mechanism introduced above admits a natural interpretation in geometric terms. The Jensen-Shannon distance d_{JS} induces a bounded metric structure on the interior of the probability simplex Δ°, transforming the space of observer-induced distributions into a well-defined statistical manifold.

Each observer O_i produces a normalized distribution $p_i \in \Delta^\circ$ through the projection mechanism defined in Equation (3). The ensemble of observations therefore corresponds to a finite cloud of points in $\left(\Delta^\circ, d_{\mathrm{JS}}\right)$.

The exact collective state p^{F} defined as the empirical Fréchet mean

$$p^{\mathrm{F}} = \arg\min_{p \in \Delta^\circ} \sum_{i=1}^{N} d_{\mathrm{JS}}^2\left(p_i, p\right)$$

represents the variational center of this observer ensemble. When a closed-form empirical surrogate is needed, we use the geometric overlap estimator p^{G} of Equation (10).

In this representation, the emergence of objectivity corresponds to a contraction phenomenon in the information-geometric manifold: as the number of independent observers increases, the dispersion of $\{p_i\}$ around the barycenter decreases and the collective state stabilizes.

This process is conceptually analogous to the emergence of classical objectivity in decoherence-based approaches such as quantum Darwinism, where redundant environmental records allow multiple observers to infer a common classical state. In the present framework, however, the stabilization mechanism is formulated directly at the level of probability distributions rather than Hilbert-space dynamics.

The resulting picture can therefore be interpreted as a geometric description of multi-observer decoherence: classical objectivity emerges as the stable barycentric structure induced by redundant observational projections in the probability simplex.

2.7. Null-Test Protocol: Permutation Baseline

A central methodological question is whether the observed barycentric clustering and the resulting cross-domain distinguishability hierarchy reflect genuine structural alignment between observers, or whether they could arise trivially from any collection of normalized distributions with similar marginal properties.

To address this issue we introduce a *permutation-based null test* that is applied uniformly across all empirical domains analyzed in this work. The purpose of the test is to determine whether the observed Jensen-Shannon geometry between observers exceeds what would be expected if the internal ordering of spectral or spatial bins carried no shared physical information.

Definition 4 (Permutation null distribution). Let $\{p_i\}_{i=1}^{N}$ denote the observed set of observer-induced probability distributions defined on a common grid $\{x_k\}_{k=1}^{K}$. For each permutation index $b=1,\cdots,B$ we construct a surrogate ensemble as follows:

1) For each observer i, generate a surrogate distribution $\tilde{p}_i^{(b)}$ by randomly permuting the bin indices k of p_i. This operation preserves the marginal histogram of probability values for each observer while destroying the bin-to-bin alignment between observers.

2) Compute the geometric barycenter $\tilde{p}^{*(b)}$ of the surrogate ensemble $\left\{\tilde{p}_i^{(b)}\right\}_{i=1}^{N}$.

3) Compute the mean pairwise Jensen-Shannon distance

$$\bar{d}_{\mathrm{JS}}^{(b)}=\frac{2}{N(N-1)}\sum_{i<j}d_{\mathrm{JS}}\left(\tilde{p}_i^{(b)},\tilde{p}_j^{(b)}\right).$$

The permutation null distribution is defined as the empirical distribution of the statistics $\left\{\bar{d}_{\mathrm{JS}}^{(b)}\right\}_{b=1}^{B}$.

In the present paper, the null statistic retained for inference is $\bar{d}_{\mathrm{JS}}^{(b)}$; the surrogate barycenter, which is computed only as an auxiliary collective summary and is not used directly in the reported significance criterion.

Definition 5 (Non-triviality criterion). Let $\bar{d}_{\mathrm{JS}}^{\mathrm{obs}}$ denote the observed mean pairwise Jensen-Shannon distance of the original observer ensemble. The multi-observer geometry is declared *non-trivial* at a significance level α if

$$\bar{d}_{\mathrm{JS}}^{\mathrm{obs}} \notin \left[q_{\alpha/2}^{\mathrm{null}}, q_{1-\alpha/2}^{\mathrm{null}} \right], \tag{13}$$

where $q_{\alpha/2}^{\mathrm{null}}$ and $q_{1-\alpha/2}^{\mathrm{null}}$ are the empirical quantiles of the permutation distribution.

Remark. The permutation procedure preserves the marginal distribution of probability values for each observer while destroying the *structural correspondence* between bins across observers. A statistically significant deviation from the permutation baseline therefore indicates that the observed Jensen-Shannon geometry reflects genuine cross-observer alignment in the underlying spectral or spatial structure, rather than an artifact of normalization, finite support, or discretization.

Throughout this work we use $B = 5000$ permutations and a significance level $\alpha = 0.05$.

Resolution limit of permutation *p*-values. Permutation *p*-values reported in this work are computed using $B = 5000$ surrogate realizations. For a two-sided permutation test this implies a minimum attainable significance level of

$$p_{\min} = \frac{2}{B} = 4 \times 10^{-4}.$$

When the observed statistic lies beyond all sampled surrogate values, the permutation estimate therefore saturates this resolution limit. In such cases the significance is reported conservatively as $p \le 4 \times 10^{-4}$ rather than as an approximate equality.

Remark. The permutation null test evaluates whether the *structural geometry* of the observer ensemble exceeds a random baseline. This procedure is distinct from bootstrap resampling of observers, which measures the sampling variability of the barycenter given a fixed set of probability distributions. Both procedures are reported in the empirical sections when relevant.

2.8. Emergent Time as Informational Displacement

A central programmatic claim of the IFR framework is that time is not a primitive quantity, but emerges as the cumulative distinguishability of successive stabilized collective states. We define it formally here as a target for a dedicated companion study; the present paper does not test this definition empirically.

2.8.1. Sequential Collective States

In this subsection, the superscript $*$ denotes a generic sequential collective state and is used only programmatically; it should not be confused with either the exact Fréchet minimizer p^{F} or the geometric overlap estimator p^{G} introduced in

Section 2.4.

Consider an ordered sequence of collective states $\left\{p^{*(n)}\right\}_{n\geq 0}$, each obtained as the barycenter of the observer set available at step n. Define the incremental informational displacement:

$$\Delta T_n := d_{\text{JS}}\left(p^{*(n)}, p^{*(n-1)}\right), \tag{14}$$

and the cumulative emergent time:

$$T_n := \sum_{k=1}^{n} \Delta T_k = \sum_{k=1}^{n} d_{\text{JS}}\left(p^{*(k)}, p^{*(k-1)}\right). \tag{15}$$

This arc-length definition is consistent with the Riemannian structure of statistical manifolds in information geometry [10] and formalizes the intuition that *time measures irreducible informational change* between successive collective states. Its relationship to physical time parameters in established dynamical theories requires independent investigation and is deferred.

2.8.2. Arrow of Time and Compression Limits

When observation cannot be fully compressed into a single invariant representation, $\left\{p^{*(n)}\right\}$ continues to move in the simplex and T_n increases. In this programmatic view, the arrow of time corresponds to the direction of non-redundant informational accumulation. Because $d_{\text{JS}} \geq 0$, a literal reversal of emergent-time increments is impossible within the same assimilation process; time inversion must be understood as inversion of the assimilation dynamics, which is generically ill-posed due to many-to-one compression.

2.9. Extensions and Connections

The definitions above constitute the complete mathematical backbone required for the empirical pipeline. The following connections to broader frameworks are noted for interpretive completeness; they do not introduce additional empirical claims.

2.9.1. Variational Formulation

The barycenter definition Equation (9) can be rewritten as the minimizer of an informational action:

$$\mathcal{S}_N\left[p\right] := \sum_{i=1}^{N} w_i D_{\text{JS}}\left(p_i \parallel p\right), \quad p \in \Delta^{\circ}. \tag{16}$$

A regularized path functional encoding a tradeoff between instantaneous fit and temporal smoothness is:

$$\mathcal{A}\left[p(\cdot)\right] = \int_{N_0}^{N_1} \left(\sum_{i\leq N} w_i D_{\text{JS}}\left(p_i \parallel p(N)\right) + \lambda \left\| \frac{\mathrm{d}p}{\mathrm{d}N} \right\|_{JS}^{2} \right) \mathrm{d}N, \tag{17}$$

where $\lambda > 0$ controls resistance to abrupt informational jumps.

2.9.2. Holographic Entropy Bound

Let $p^{(N)}$ be the stabilized collective state with Shannon entropy

$H\left(p^{(N)}\right) := -\sum_k p_k^{(N)} \log p_k^{(N)}$. The operational capacity constraint

$$H\left(p^{(N)}\right) \le \mathcal{C} \tag{18}$$

is conceptually aligned with holographic entropy arguments [1]-[5], and is interpreted here as an operational bound on the manifestable degrees of freedom under the chosen observational channel. This connection is presented as a structural analogy, not a derivation.

2.9.3. Categorical Perspective

An observer O induces a functor $\mathcal{F}_O : \mathbf{Sub} \to \mathbf{Prob}$ mapping the substrate category **Sub** (objects: $\Phi \in \mathcal{H}$; morphisms: admissible transformations) to the probability category **Prob** (objects: probability simplexes with d_{JS} ; morphisms: stochastic maps) via $\mathcal{F}_O(\Phi) = p_O$. Objectivity in this language corresponds to stable colimit- like constructions (barycenters) compatible across observer channels, formalizing the absence of a privileged observer. This categorical language is presented as a possible direction for future formalization.

Operational definitions. For the empirical sections, three terms are used in a strictly operational sense.

Observer. An observer is any measurement channel, processing configuration, temporal epoch, instrumental mode, detector, or catalog split that induces a normalized probability distribution $p_i \in \Delta^\circ$ on a shared representational space.

Redundant observation. An observation is redundant when distinct observers impose overlapping informational constraints on the same target structure, so that their induced distributions are expected to cluster in Jensen-Shannon geometry even if the channels are not identical.

Shared underlying structure. Shared underlying structure denotes the common physical or statistical organization responsible for that clustering. Operationally, it is inferred when independent or heterogeneous observers, once mapped to a common grid and normalized consistently, yield distances significantly below an appropriate permutation baseline and a stable collective summary.

Common Methods

To facilitate comparison across domains, all empirical instantiations follow the same pipeline up to the domain-specific observer construction.

Dataset selection. For each domain we select publicly available datasets with at least two meaningfully comparable observer channels (detectors, smoothing configurations, epochs, instrumental modes, or catalog partitions), and we restrict the analysis to the spectral or summary range relevant to that domain.

Preprocessing. Each raw observable is converted into a non-negative spectral or histogram-like representation on its native support. When needed, standard preprocessing is applied first (e.g. band restriction, smoothing, absolute-value recoding, or PSD estimation by the Welch method) before normalization.

Master-grid construction. All observers within a given analysis are projected onto a common master grid so that Jensen-Shannon distances are computed only between distributions defined on the same representational support.

Normalization. Each observer representation is normalized to unit mass, so that every empirical state satisfies $p_i \geq 0$ and $\sum_k p_i(x_k) = 1$ on the common grid. The analysis therefore targets shape geometry rather than absolute amplitude.

Weighting and collective summaries. Unless otherwise stated, observer weights are uniform. Three collective summaries are then distinguished: the exact empirical Fréchet minimizer p^{F} (Equation (9)), the closed-form geometric overlap estimator p^{G} (Equation (10)), and the arithmetic mean $\overline{p}$ (Equation (11)).

Bootstrap settings. Where bootstrap summaries are reported, the resampling unit and statistic are those stated locally in the corresponding domain subsection. Bootstrap intervals are used only as stability diagnostics for the reported statistic and are not assumed to coincide automatically with the observed cross-observer JS distances unless explicitly stated.

Permutation null tests. All empirical domains are additionally evaluated with the common permutation protocol of Definition 4: bins are permuted within observer representations to preserve marginals while destroying cross-observer alignment. The observed geometry is then compared with the resulting null baseline through the same JS metric.

Interpretive rule. Throughout the empirical sections, low within-domain distances and stable collective summaries are interpreted as evidence of redundant observational access to a shared underlying structure, whereas larger separations indicate structured heterogeneity of the observer family rather than, by themselves, any failure of the framework.

3. Empirical Instantiations I: Gravitational-Wave Open Data (GWOSC)

This section tests the multi-observer stabilization principle in the gravitational-wave domain using publicly available data and fully reproducible pipelines. Each interferometer is treated as an independent observer inducing a normalized spectral probability distribution on a common frequency grid. No claim is made about new gravitational-wave physics: the analysis concerns only the information-geometric structure of observer-induced probability representations.

3.1. Observer-Dependent Spectral States

Each detector (observer) i is represented by a normalized spectral probability density $p_i(f)$ on a common frequency grid $\{f_k\}_{k=1}^{K}$, obtained from the band-limited strain power spectral density (PSD) via the Welch method [15] and normalized as

$$p_i(f_k) \geq 0, \quad \sum_{k=1}^{K} p_i(f_k) = 1. \tag{19}$$

This representation discards absolute PSD amplitude and retains only the *spectral shape* as a probability distribution. Jensen-Shannon geometry therefore quantifies *shape distinguishability* between detectors independently of absolute sensitivity.

3.2. Two-Observer Case: GW150914-v2 (H1/L1, 30 - 150 Hz)

For GW150914-v2 in the 30 - 150 Hz band, we consider two observers, p_{H1} and p_{L1}, defined on a shared frequency grid. The detector-to-detector JS distance and the distances to the geometric overlap estimator p^{G} and arithmetic mean $\bar{p}$ are reported in **Table 1**.

Table 1. GW150914-v2 (30 - 150 Hz): two-observer Jensen-Shannon geometry. All distances in nats.

Quantity	Value
$d_{\mathrm{JS}}\left(p_{H1}, p_{L1}\right)$	0.3655
$d_{\mathrm{JS}}\left(p_{H1}, p^{\mathrm{G}}\right)$	0.1971
$d_{\mathrm{JS}}\left(p_{L1}, p^{\mathrm{G}}\right)$	0.1870
$d_{\mathrm{JS}}\left(p_{H1}, \bar{p}\right)$	0.1876
$d_{\mathrm{JS}}\left(p_{L1}, \bar{p}\right)$	0.1925
Local ratio $d\left(p_{H1}, p^{\mathrm{G}}\right) / d\left(p_{H1}, \bar{p}\right)$	0.950
Local ratio $d\left(p_{L1}, p^{\mathrm{G}}\right) / d\left(p_{L1}, \bar{p}\right)$	0.971

At the level of individual detector-to-center distances, the geometric overlap estimator p^{G} is slightly closer to H1 than the arithmetic mean and slightly farther from L1. These local shifts reflect the overlap-selective behavior of Equation (10), but they should not be described as *contraction* in the strict sense used later in Section 9.2. Throughout this paper, contraction is defined only by the global dispersion ratio $\rho = \mathcal{V}_N\left(p^{\mathrm{G}}\right) / \mathcal{V}_N\left(\bar{p}\right)$: for GW150914 with $N = 2$, $\rho = 1.010$, so no strict contraction is observed in that sense.

Null test. Using the permutation protocol of Definition 4 with $B = 5000$ surrogate realizations, the observed H1-L1 distance is $d_{\mathrm{JS}}^{\mathrm{obs}} = 0.3655$, whereas the null distribution gives $\langle d_{\mathrm{JS}} \rangle_{\mathrm{null}} = 0.7746 \pm 0.0430$ nats, corresponding to $z = -9.51$. The observed two-detector geometry is therefore far more clustered than expected under random spectral-bin permutations, indicating genuine shared structure rather than a normalization artifact (**Figure 2**).

3.3. Internal Validation via Multi-Band Observers ($N = 6$)

To test internal consistency and the effect of bandwidth selection, we treated six band-limited reconstructions of GW150914-v2 as independent observers,

$$\left\{H1_{10-1024}, H1_{30-300}, H1_{30-150}, L1_{10-1024}, L1_{30-300}, L1_{30-150}\right\},$$

all projected onto a common master grid in the 30 - 150 Hz band and assigned uniform weights $w_i = 1/6$.

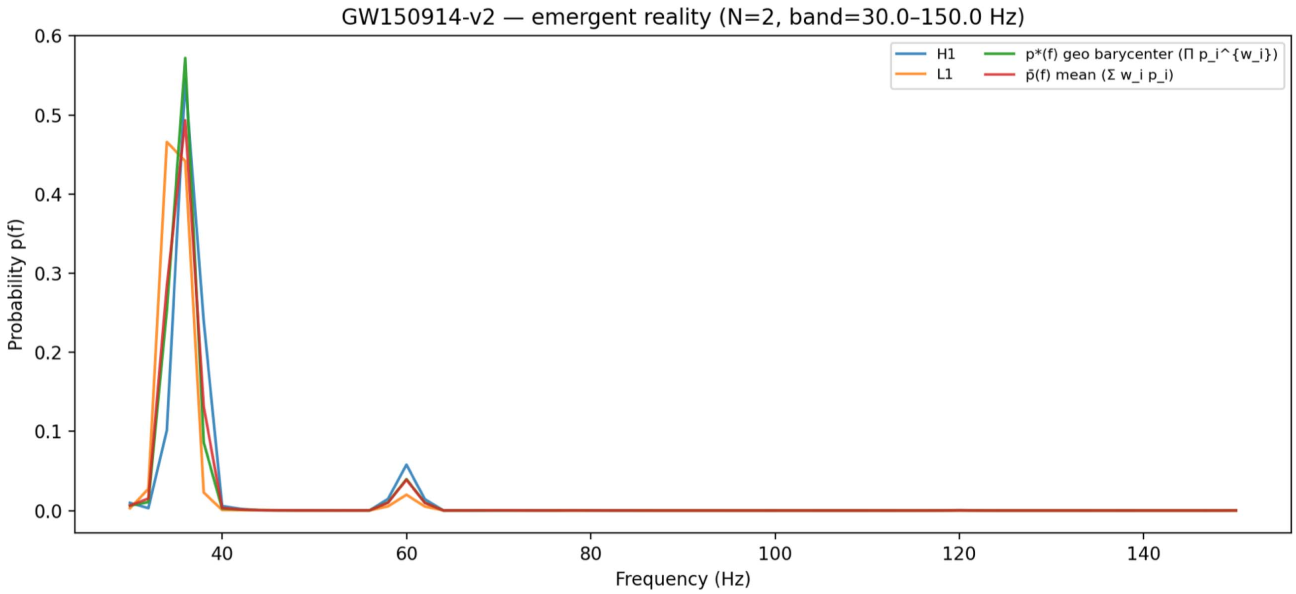

Figure 2. GW150914-v2 (30 - 150 Hz): $p_{H1}(f)$, $p_{L1}(f)$, geometric overlap estimator $p^{\mathrm{G}}(f)$, and arithmetic mean $\overline{p}(f)$ for the two-observer case.

Table 2. GW150914-v2 multiband validation ($N=6$, projected to 30 - 150 Hz). Distances in nats.

Observer	$d\left(p_i, p^{\mathrm{G}}\right)$	$d\left(p_i, \overline{p}\right)$
$H1_{10-1024}$	0.3236	0.2344
$H1_{30-150}$	0.1691	0.0899
$H1_{30-300}$	0.1702	0.1011
$L1_{10-1024}$	0.4311	0.3542
$L1_{30-150}$	0.2914	0.3740
$L1_{30-300}$	0.2895	0.3792
$\bar{d}_{\mathrm{JS}}$ (pairwise)	0.3779	
$d_{\mathrm{JS}}^{\max}$ (pairwise)	0.6494	

Two features are evident from **Table 2**. First, the broadband observers ($H1_{10-1024}$ and $L1_{10-1024}$) lie systematically farther from the barycenter than their narrowband counterparts, indicating that the additional low-frequency instrumental content acts as an outlier component in JS geometry. Second, within each detector, the two narrowband reconstructions (30 - 150 Hz and 30 - 300 Hz) cluster very tightly, while the broadband 10 - 1024 Hz reconstructions remain more peripheral. This shows that the spectral shape in the physically relevant 30 - 150 Hz window is robustly recovered across acquisition-band choices, even when the broader broadband reconstructions remain more peripheral in JS geometry. Together, these results support the stabilization picture: aligned observers cluster near the collective center, whereas structurally discrepant ones remain more peripheral (**Figure 3**).

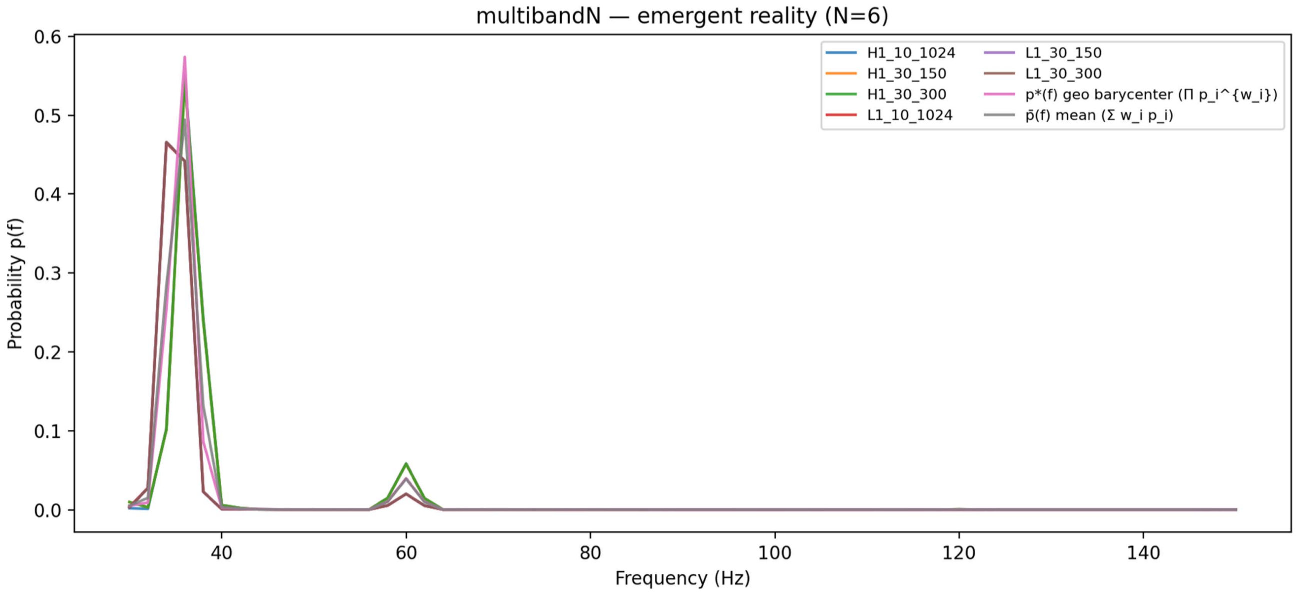

Figure 3. GW150914-v2 multiband validation in the 30 - 150 Hz band: six observers and collective geometric overlap estimator $p^{\mathrm{G}}(f)$.

3.4. GWOSC Multi-Detector Test: GW170817-v2 ($N = 3$ Observers)

We next apply the emergent-reality construction to GW170817-v2 cleaned strain segments (16 kHz, 2048 s) from the three interferometers Hanford (H1), Livingston (L1), and Virgo (V1), using uniform weights $w_i = 1/3$ (**Table 3**).

Table 3. GW170817-v2 ($N = 3$): multi-observer JS geometry. All distances in nats.

Quantity	Geometric p^{G}	Arithmetic $\bar{p}$
$d(p_{H1},\cdot)$	0.3012	0.3485
$d(p_{L1},\cdot)$	0.4510	0.4309
$d(p_{V1},\cdot)$	0.5992	0.5515
$\bar{d}_{\mathrm{JS}}$ (pairwise)	0.6774	
$d_{\mathrm{JS}}^{\max}$ (pairwise)	0.8257	

The large pairwise distances ($\bar{d}_{\mathrm{JS}} \approx 0.68$ nats) reflect the known sensitivity asymmetry of the H1/L1/V1 network at the epoch of GW170817, with Virgo substantially less sensitive in the relevant band. Relative to the arithmetic mean, the geometric overlap estimator moves closer to H1 and farther from V1, while L1 remains intermediate. This is consistent with the overlap-selective character of the geometric estimator: spectral regions shared by H1 and L1 are emphasized, whereas bins in which V1 departs from the LIGO consensus are comparatively down-weighted.

Null test. Applying Definition 4 with $B = 5000$ surrogate realizations, the observed mean pairwise distance is $\bar{d}_{\mathrm{JS}}^{\mathrm{obs}} = 0.6774$, while the null baseline gives $\langle d_{\mathrm{JS}} \rangle_{\mathrm{null}} = 0.8289 \pm 0.0110$ nats, corresponding to $z = -13.8$. The three-detector configuration is thus significantly more structured than expected under permutation, with H1 and L1 forming the closest pair and V1 remaining more distant for non-trivial geometric reasons (Figures 4-6).

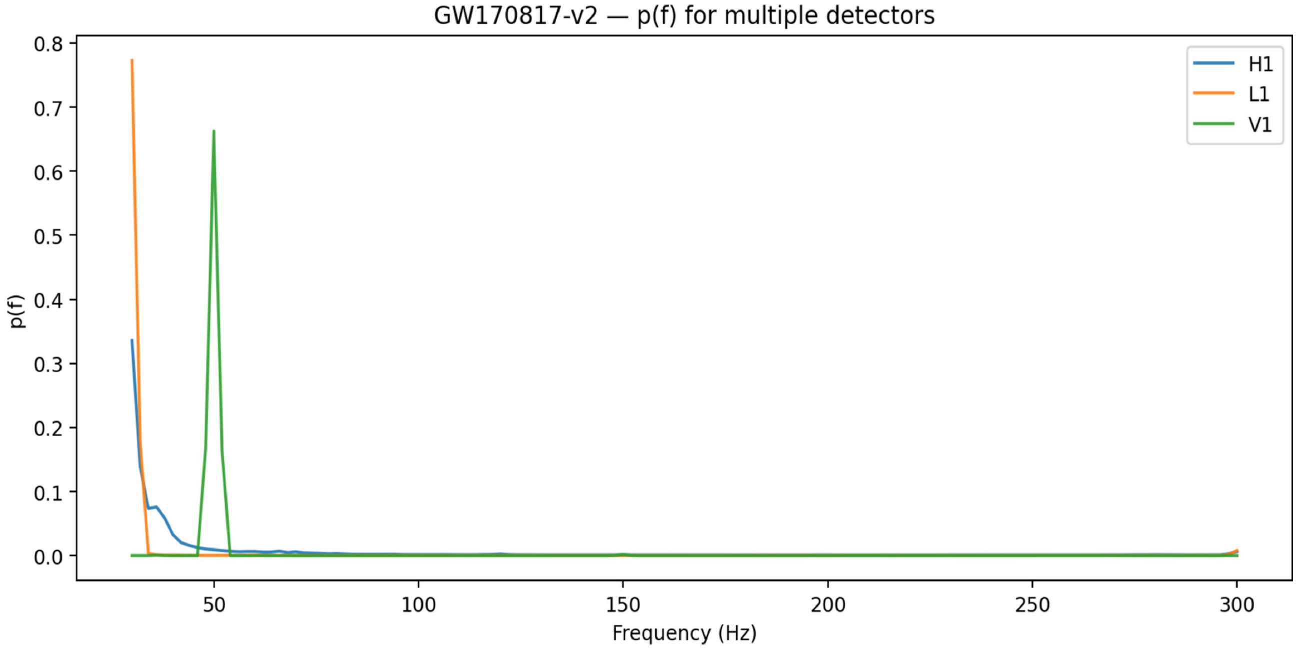

Figure 4. GW170817-v2: normalized PSD probability densities $p(f)$ for H1, L1, and V1.

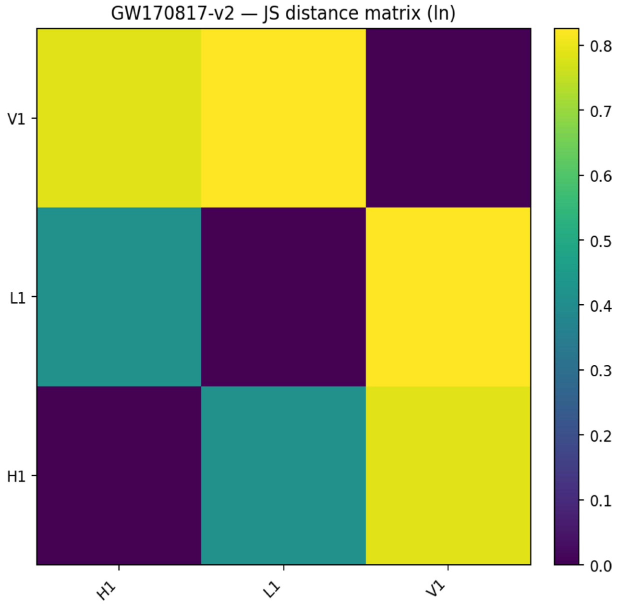

Figure 5. GW170817-v2: Jensen-Shannon distance matrix for the H1/L1/V1 observer ensemble.

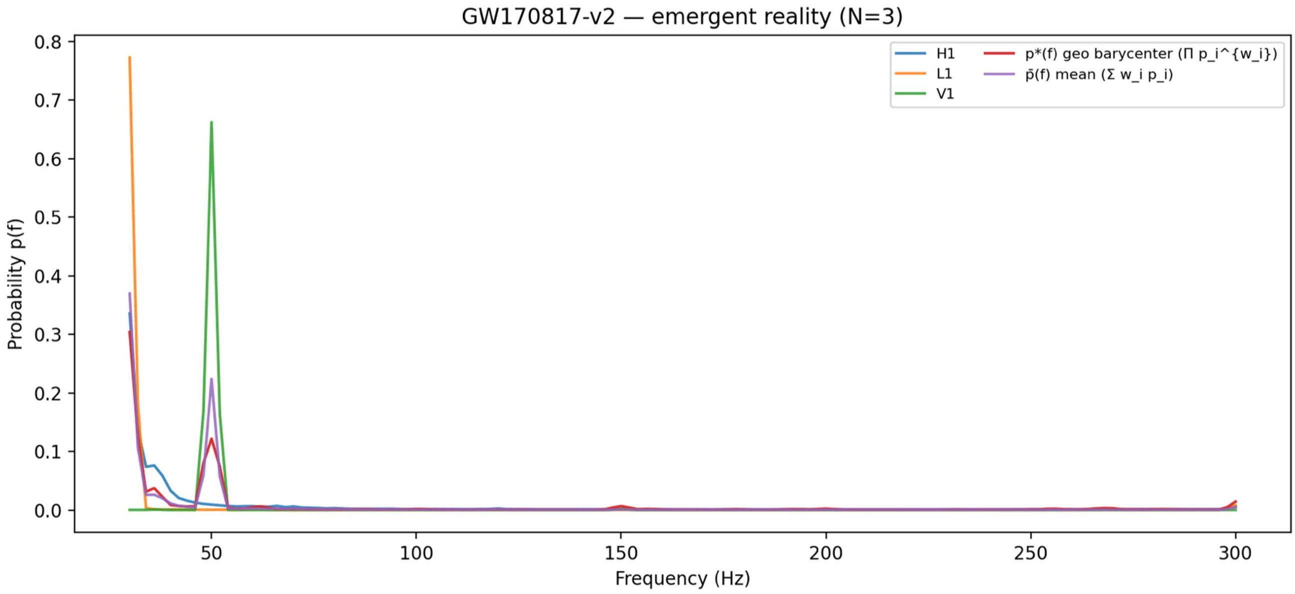

Figure 6. GW170817-v2: observer distributions, geometric overlap estimator $p^{G}(f)$, and arithmetic mean $\overline{p}(f)$ for the three-detector ensemble.

4. Cross-Event Information Geometry: GW150914 vs GW170817

A testable consequence of the interference-first framework is that physically distinct events, when represented by multi-observer collective states in a shared probability simplex, should be geometrically separable in the Jensen-Shannon metric, with the degree of separation reflecting the informational distinctiveness of their observer ensembles. Here we compare two events of different astrophysical type—GW150914-v2 (binary black hole, BBH) and GW170817-v2 (binary neutron star, BNS)—by embedding them in a common Jensen-Shannon geometry through a shared frequency band and a common simplex representation, and we test whether their emergent collective states remain distinguishable relative to a permutation baseline.

Remark. The cross-event JS distance reported here primarily captures differences in *detector noise spectral shape* at the two observing epochs, rather than differences in the astrophysical source signals themselves. Since GW150914 and GW170817 were recorded roughly two years apart, the corresponding detector configurations and noise floors are not the same. Accordingly, the cross-event geometry should be interpreted as a measure of the information-geometric distinguishability of the observational contexts, not of source classes as such.

4.1. Common Simplex Embedding

For each event E and detector/observer i, we construct a normalized spectral probability distribution on a common frequency grid $\{f_k\}_{k=1}^{K}$:

$$p_{E,i}(f_k) \geq 0, \quad \sum_{k=1}^{K} p_{E,i}(f_k) = 1. \tag{20}$$

All detectors and both events are projected onto the same 30 - 300 Hz band and the same grid ($K = 4096$ bins), so that all $p_{E,i}$ belong to a single probability simplex $\mathcal{P}$. This common embedding is required for a meaningful Jensen-Shannon comparison between event-level geometric estimators.

4.2. Event-Level Emergent Reality

For each event E, with weights $w_{E,i} \geq 0$ satisfying $\sum_i w_{E,i} = 1$ (uniform in the present implementation), we define the weighted geometric overlap estimator

$$p_E^{\mathrm{G}}(f_k) = \frac{\prod_{i=1}^{N_E} p_{E,i}(f_j)^{w_{E,i}}}{\sum_{j=1}^{K} \prod_{i=1}^{N_E} p_{E,i}(f_j)^{w_{E,i}}}. \tag{21}$$

GW150914-v2 contributes $N_E = 2$ observers (H1, L1), whereas GW170817-v2 contributes $N_E = 3$ observers (H1, L1, V1). Both event-level geometric estimators therefore lie in the same simplex $\mathcal{P}$ and can be compared directly.

4.3. Cross-Event Distance and Meta-Barycenter

The informational separation between two events is defined as

$$d_{\mathrm{JS}}(E_1, E_2) := d_{\mathrm{JS}}\left(p_{E_1}^{\mathrm{G}}, p_{E_2}^{\mathrm{G}}\right). \tag{22}$$

At the next level, we define the class-level meta-barycenter

$$p^{\star}(f_k) = \frac{\prod_E \left(p_E^{\mathrm{G}}(f_j)\right)^{W_E}}{\sum_{j=1}^{K} \prod_E \left(p_E^{\mathrm{G}}(f_j)\right)^{W_E}}, \quad \sum_E W_E = 1. \tag{23}$$

The meta-barycenter $p^{\star}$ is the collective JS-optimal representative of the two-event ensemble; its distances from the individual event-level geometric estimators quantify how far each observational context lies from the global consensus.

4.4. Results: GW150914-v2 vs GW170817-v2, 30 - 300 Hz (Table 4)

Table 4. Cross-event information geometry on a common 30 - 300 Hz simplex ($K = 4096$ bins). All distances in nats.

Quantity	Value
$d_{\mathrm{JS}}\left(p_{\mathrm{GW150914}}^{\mathrm{G}}, p_{\mathrm{GW170817}}^{\mathrm{G}}\right)$	0.6517
$d_{\mathrm{JS}}\left(p_{\mathrm{GW150914}}^{\mathrm{G}}, p^{\star}\right)$	0.2604
$d_{\mathrm{JS}}\left(p_{\mathrm{GW170817}}^{\mathrm{G}}, p^{\star}\right)$	0.4872
Asymmetry ratio d_{170817}/d_{150914}	1.87

The cross-event distance $d_{\mathrm{JS}} \approx 0.652$ nats shows that the two observational contexts occupy well-separated regions of the common 30 - 300 Hz probability simplex.

The asymmetry in the distances to the meta-barycenter is also informative. GW170817-v2 lies substantially farther from the two-event consensus than

GW150914-v2 (asymmetry ratio ≈ 1.87), consistent with the fact that the GW170817 network includes Virgo, whose spectral shape differs markedly from the two LIGO detectors. This is in line with the multi-detector structure reported in Section 3, where $d\left(p_{V1}, p^{G}\right)$ is the largest among the three GW170817 observers.

Null test. At the event-barycenter level, using Definition 4 with $B = 5000$ surrogates, the observed cross-event distance is $d_{\mathrm{JS}}^{\mathrm{obs}} = 0.6517$, compared with a null expectation of $\langle d_{\mathrm{JS}} \rangle_{\mathrm{null}} = 0.7917 \pm 0.0050$ nats, yielding $z = -28.24$ and $p_{\mathrm{two}} \approx 4 \times 10^{-4}$. The separation between the two event barycenters is therefore far stronger than expected under permutation, confirming that GW150914-v2 and GW170817-v2 occupy distinct regions of the common Jensen-Shannon geometry (Figure 7).

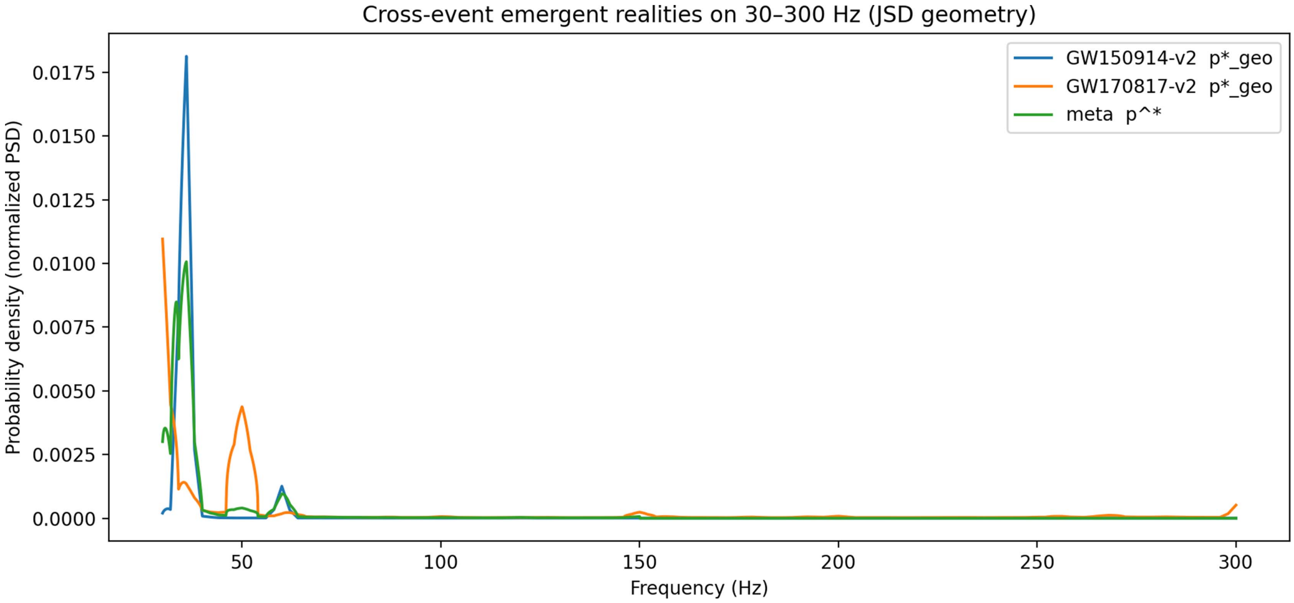

Figure 7. Cross-event embedding of GW150914-v2 and GW170817-v2 in a common 30 - 300 Hz simplex, with event-level geometric estimators and meta-barycenter $p^{*}(f)$.

5. Empirical Instantiations II: CMB and HRV

This section examines the stabilization principle in two independent domains: cosmology (CMB) and physiology (HRV). Both were analyzed previously in [7] within the same information-geometric framework; here they are retained as validated instantiations and recast in the fully multi-observer formalism of Section 2.

For each domain, we report two complementary analyses. First, a *parsimony analysis*, carried over from [7], measures the Jensen-Shannon (JS) distance between an empirical spectrum and a parsimonious reference family, thereby locating the domain within the coherence hierarchy. Second, a *multi-observer stability analysis*, new in the present work, treats independent processing configurations or temporal segments as observers and computes the empirical Fréchet barycenter, directly testing the stabilization prediction of Theorem 1.

In all cases, observer-induced probability distributions are obtained by normalizing power spectral densities over a common grid according to Equation (19), and all JS distances are reported in natural units (nats).

5.1. Cosmological Domain: CMB

Data and observer construction. We use the Planck 2018 legacy angular power spectra TT, EE, and TE [16]. Each spectrum C_ℓ is evaluated on a common multipole grid and normalized as

$$p_i\left(\ell_k\right)=\frac{\left|C_\ell^{(i)}\left(\ell_k\right)\right|}{\sum_k\left|C_\ell^{(i)}\left(\ell_k\right)\right|}. \tag{24}$$

For the parsimony analysis, the reference model $q(\ell)$ is a Gaussian envelope matched to the empirical mean and variance of the spectrum. For the multi-observer analysis, different smoothing configurations ($\Delta\ell\in\{20,30\}$, $\sigma\in\{0.5,1.0,1.5\}$) are treated as independent observers.

Parsimony results. Table 5 reports the JS distances between the empirical Planck 2018 spectra and their parsimonious Gaussian-envelope references, together with distances to the best-fit ΛCDM (CAMB) prediction. These values are reproduced from [7]; bootstrap details are given there.

Table 5. CMB: Jensen-Shannon distances between Planck 2018 spectra and parsimonious reference models. $\sigma=0.5$ (optimal); $\sigma=1.0$ (sensitivity check). CAMB values use the best-fit ΛCDM prediction as reference. All distances in d_{JS} (natural units).

Spectrum	Reference	$\sigma=0.5$	$\sigma=1.0$
TT	Gaussian envelope	0.0021	0.015
EE	Gaussian envelope	0.0078	0.030
TE	Gaussian envelope	0.0375	0.118
TT	CAMB ΛCDM	0.004	—
EE	CAMB ΛCDM	0.018	—
TE	CAMB ΛCDM	0.031	—

TT and EE lie at $d_{\text{JS}}\sim10^{-3}\text{-}10^{-2}$ nats from their optimal envelopes, placing them deep in the low-curvature region of the coherence hierarchy. TE shows larger divergence because of its sign structure; when modeled through a two-channel (sign + magnitude) decomposition, the residual divergence returns to the same low-curvature regime. Comparison with CAMB ΛCDM predictions further confirms that the empirical spectra remain close to the theoretical submanifold, consistent with the high compressibility of the acoustic peak structure.

Multi-observer stability. The sweep over smoothing configurations (**Figure 8**) shows a stable minimum near $(\Delta\ell,\sigma)=(20,0.5)$ for TT and $(30,0.5)$ for EE, identifying the regime of maximal cross-observer agreement. Operationally, this is the barycentric regime in which the JS dispersion $\mathcal{V}_N$ is minimized.

Table 6. CMB TT multi-observer stability: bootstrap summary at the optimal configuration ($\Delta\ell = 20$, $\sigma = 0.50$). Base JSD is the observed JS distance; bootstrap mean and 95% CI are from $B = 1000$ resamples [7].

Spectrum	Base d_{JS}	Boot. mean	95% CI	
			Lower	Upper
Planck TT	0.0251	0.4403	0.3886	0.4866

Bootstrap interpretation. The bootstrap summary in Table 6 does not refer to the same quantity as the cross-observer distance reported for the selected smoothing configuration. The resampling unit is the multipole bin on the common ℓ-grid, sampled with replacement after the same absolute-value normalization used in Equation (24). The bootstrapped statistic is the JS discrepancy of a resampled spectrum relative to its reference construction in the legacy CMB parsimony analysis of [7], not the observer-to-observer distance between the two final smoothed configurations displayed here. For this reason, the bootstrap mean can be much larger than the observed cross-observer JS distance: it measures the variability of a broader spectrum-to-reference discrepancy under resampling, whereas the reported observed value concerns a specific, already optimized pair of smoothing configurations.

Null test. Using $B = 5000$ surrogate realizations obtained by randomly permuting the multipole bins, the observed distance between the smoothed spectra is $d_{\text{JS}}^{\text{obs}} = 0.0021$, whereas the permutation baseline gives $\langle d_{\text{JS}} \rangle_{\text{null}} = 0.186 \pm 0.004$ with $p_{\text{two}} < 10^{-3}$. The observed value is therefore more than two orders of magnitude below the null expectation, confirming that the similarity among processing variants reflects the underlying acoustic peak structure rather than trivial normalization effects.

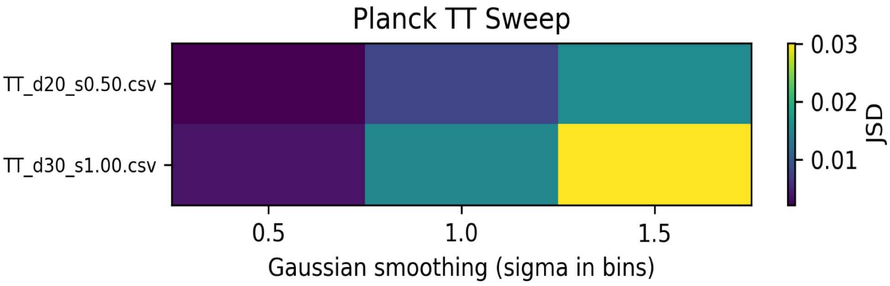

Figure 8. Jensen-Shannon distance between CMB TT observer configurations as a function of the Gaussian smoothing parameter σ .

5.2. Physiological Domain: HRV

Data and observer construction. ECG recordings are taken from the Fantasia database [17], subject f1y01. Power spectral densities are estimated with the Welch method [15] using a Hann window. The frequency axis is restricted to the standard HRV band $[0.003, 0.4]$ Hz and normalized according to Equation (19).

Two observer families are considered:

1) **Model observers (parsimony analysis):** the empirical spectrum $p(f)$ is compared with Gaussian mixture models of increasing order (VLF + LF: 2G; VLF + LF + HF: 3G), following the Task Force band definitions [18].

2) **Epoch observers (multi-observer analysis):** the recording is segmented into 2 (2G) or 3 (3G) equal-length non-overlapping epochs; each epoch defines an independent observer whose spectral shape is compared by JS distance.

Biological substrate remark. The HRV power spectrum considered here is the frequency-domain projection of the inter-beat interval series generated by the cardiac electromechanical cycle. At the level of structural plausibility, the helical ventricular myocardial band (HVMB) description of ventricular mechanics [19], together with subsequent electromechanical analyses [20], suggests a nonlinear, anisotropic, and time-varying generator. This is precisely the regime in which the bounded and symmetric Jensen-Shannon metric is preferable to linear or KL-based measures for comparing observer-dependent spectral shapes. The present analysis does not test the HVMB model itself; it reports only the information-geometric structure of the observer-induced spectral distributions. The biological motivation is included only as a plausible structural background for the intermediate location of HRV in the cross-domain hierarchy.

Parsimony results. Table 7 reports the JS distances between the empirical HRV spectrum and fitted Gaussian mixture models, together with bootstrap summaries ($B = 1000$) reproduced from [7].

Table 7. HRV (Fantasia f1y01): Jensen-Shannon distances and bootstrap summary for 2G and 3G mixture models. ΔJSD = JSD(2G) - JSD(3G). Bootstrap 95% CI from $B = 1000$ resamples [7].

Model	Base d_{JS}	Boot. mean	Boot. sd	95% CI	
				Lower	Upper
2G	0.0857	0.4319	—	0.3482	0.5157
3G	0.0752	0.4320	0.0429	0.3474	0.5173
ΔJSD (2G - 3G)			−0.0035		

The 3G model marginally outperforms the 2G model (ΔJSD = −0.0035), but the bootstrap distributions overlap strongly, indicating negligible advantage from the higher-order representation. This supports JS-based parsimony: the 2G model already captures the dominant spectral structure with minimal additional complexity.

For Fantasia f1y01, $d_{\text{JS}}^{3G} = 0.0752$ nats, placing HRV roughly one order of magnitude above the CMB TT value ($d_{\text{JS}} = 0.0021$ nats) in the coherence hierarchy. By contrast, the MIT-BIH Arrhythmia record (subject 100) yields $d_{\text{JS}} \approx 0.289$, consistent with stronger arrhythmic variability pushing the spectrum farther from a constrained mixture representation.

Bootstrap interpretation. The bootstrap values in Table 7 must likewise be distinguished from the epoch-to-epoch observer distances reported later in Table

8. The resampling unit is the frequency bin of the normalized HRV power spectrum on the common grid, sampled with replacement within the legacy parsimony analysis of [7]. The bootstrapped statistic is the JS discrepancy between the resampled empirical spectrum and the fitted Gaussian-mixture model (2G or 3G), not the JS distance between different temporal epochs treated here as observers. Accordingly, the bootstrap means near 0.43 are not expected to match the much smaller epoch-to-epoch distances ($\sim 10^{-2}$): the former quantify model-fit variability under resampling, whereas the latter quantify cross-epoch agreement within a single subject after normalization.

Multi-observer epoch stability. Table 8 reports pairwise JS distances between temporal-epoch observers.

Table 8. Jensen-Shannon distances between HRV epoch observers (Fantasia dataset).

Observer pair	d_{JS} (nats)
Epoch 1 vs Epoch 2	0.0217
Epoch 1 vs Epoch 3	0.0314
Epoch 2 vs Epoch 3	0.0246

These values indicate low dispersion among temporal observers, consistent with a stable underlying spectral organization. A reduction in mean pairwise distance from 2G to 3G segmentations would indicate increased redundancy and reduced observer disagreement; Figure 9 displays this comparison with bootstrap uncertainty.

Null test. Applying Definition 4 with $B = 1000$ surrogate realizations for each epoch pair in Table 8, the observed distances remain well outside the central region of the null distributions. These permutation results concern the epoch-to-epoch observer geometry only. They should not be conflated with the bootstrap summaries of Table 7, which refer instead to spectrum-to-model discrepancies in the legacy parsimony analysis. Together, the two analyses indicate that the HRV spectrum is both parsimoniously representable at low mixture order and internally stable across temporal observer segments.

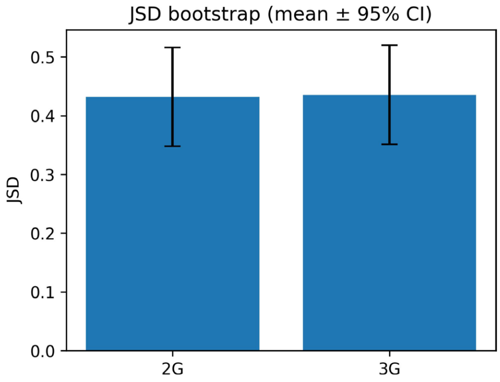

Figure 9. Jensen-Shannon distances for HRV spectral distributions under 2G and 3G segmentations, with bootstrap 95% confidence intervals.

5.3. Cross-Domain Position of CMB and HRV

Within the cross-domain distinguishability hierarchy of Section 13, CMB and HRV occupy the low-dispersion end of the spectrum. The ordering established in [7]

$$d_{\mathrm{JS}}\left(p_{\mathrm{CMB}},\mathcal{Q}_{\mathrm{CMB}}\right)\ll d_{\mathrm{JS}}\left(p_{\mathrm{HRV}},\mathcal{Q}_{\mathrm{HRV}}\right)\ll d_{\mathrm{JS}}\left(p_{\mathrm{JWST}},\mathcal{Q}_{\mathrm{JWST}}\right), \tag{25}$$

is reproduced and extended here within the multi-observer framework. CMB distances ($\sim 10^{-3}$ nats) are roughly two orders of magnitude smaller than gravitational-wave cross-event distances ($\sim 10^{-1}$ - 10^{0} nats), while HRV occupies an intermediate position.

This ordering is not interpreted as evidence of common microscopic mechanisms. Rather, it reflects differences in compressibility: the CMB angular power spectrum, being a full-sky integral over $\sim 10^{7}$ pixels, averages out most observer-dependent processing differences; HRV spectra, derived from finite physiological recordings, retain greater observer-level variability; and JWST spectra, with their multimodal line structure, occupy the high-curvature end of the JS geometry. The hierarchy is therefore interpretable in domain-specific terms and does not require a unified causal explanation across domains.

6. Empirical Instantiations III: Astronomical Spectroscopy (JWST)

The JWST analysis provides an independent astrophysical instantiation of the multi-observer formalism. As in the previous sections, the emphasis is on the structure of observer-induced probability distributions and their Jensen-Shannon geometry, not on new spectroscopic interpretation. No claim is made regarding source classification or emission-line physics beyond what the information-geometric representation can support.

6.1. Observer Construction: PRISM and GRATINGS as Spectral Channels

We analyze the JADES NIRSpec public line-flux catalogs [21] from the STScI MAST archive (Program ID: 01345). The PRISM and GRATINGS products are treated as two observer channels for the same set of astrophysical sources, each providing a distinct instrumental representation of the emission-line flux distribution over a shared set of $K = 21$ common lines.

Remark. PRISM and GRATINGS are instrumental modes of the same telescope (JWST/NIRSpec), not physically independent observing platforms. Their different spectral resolution and sensitivity curves induce systematic differences in line-flux ratios. Accordingly, the JS distance between them quantifies *inter-mode representational disagreement* under a shared physical emission substrate, rather than independent observations in the GWOSC sense. This makes the JWST case a complementary test of the stabilization principle under structured instrumental heterogeneity.

For each of $N = 253$ cross-matched sources, the vector of common line fluxes is normalized to a probability distribution over the $K = 21$ emission lines:

$$p_{\text{mode}}^{(s)}\left(\lambda_k\right) = \frac{\max\left(F_k^{(s,\text{mode})}, 0\right)}{\sum_{j=1}^{K} \max\left(F_j^{(s,\text{mode})}, 0\right)}, \quad p^{(s)} \in \Delta^{\circ}, \tag{26}$$

where $F_k^{(s,\text{mode})}$ is the line flux at wavelength λ_k for source s in mode $\text{mode} \in \{\text{PRISM}, \text{GRATINGS}\}$. Sources with non-positive total flux are excluded.

6.2. Per-Source Observer Disagreement

For each source s, PRISM-GRATINGS disagreement is measured by

$$d_{\text{JS}}^{(s)} = d_{\text{JS}}\left(p_{\text{PRISM}}^{(s)}, p_{\text{GRATINGS}}^{(s)}\right).$$

The resulting distribution is summarized in Table 9 and shown in Figure 10.

Table 9. JWST JADES: per-source Jensen-Shannon distance between PRISM and GRATINGS observer channels ($N = 253$ sources, $K = 21$ common lines, natural log base).

Statistic	Value (nats)
Mean $\bar{d}_{\text{JS}}$	0.3108
Median	0.1976
Minimum	0.0000
Maximum	0.8326

The wide range (from ≈0 to ≈0.83 nats) shows substantial source-to-source variability in inter-mode agreement. Sources near zero have nearly identical line-flux ratios in both modes, whereas high-distance sources exhibit strong mode dependence, plausibly driven by resolution-dependent line blending in PRISM. The fact that the mean exceeds the median indicates a positively skewed distribution, with most sources showing moderate agreement and a minority of high-disagreement outliers.

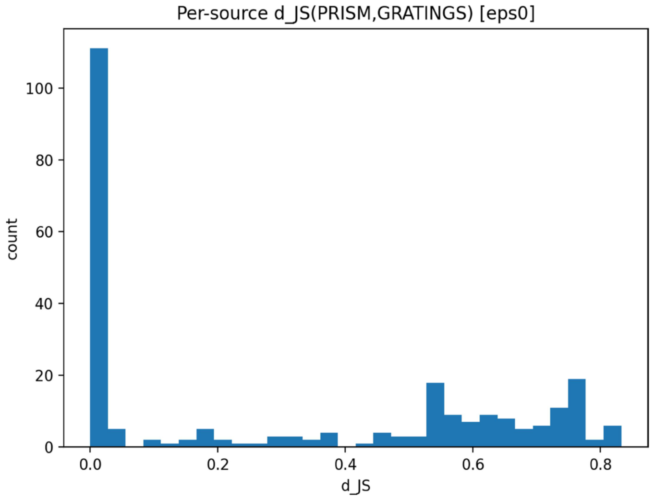

Figure 10. JWST JADES: distribution of per-source PRISM-GRATINGS Jensen-Shannon distances ($N = 253$ sources).

6.3. Global Aggregation: A1 (Arithmetic) and A2 (Geometric) Observer States

To construct global observer states from the per-source ensemble, we use two aggregation strategies corresponding to the two estimators introduced in Section 2.4.

A1: Arithmetic mean (linear baseline).

$$p_{\text{mode,mean}} = \frac{1}{N}\sum_{s=1}^{N} p_{\text{mode}}^{(s)}, \quad \text{mode} \in \{\text{PRISM}, \text{GRATINGS}\}. \tag{27}$$

A2: Dirichlet-regularized geometric overlap estimator.

Because sparse line-flux vectors can destabilize geometric aggregation through near-zero components, we apply Dirichlet smoothing:

$$\tilde{p}^{(s)}(\lambda_k) = \frac{p^{(s)}(\lambda_k) + \alpha}{1 + K\alpha}, \quad \alpha = 10^{-6}, \tag{28}$$

before computing the geometric overlap estimator. This preserves the overlap-selective character of the estimator while ensuring numerical stability (Table 10).

Table 10. JWST JADES: global A1 (arithmetic) and A2 (Dirichlet-regularized geometric) Jensen-Shannon geometry between PRISM and GRATINGS observer channels. $\text{META}_{\text{mode}}$ denotes the arithmetic midpoint of the two global observer states. Distances in nats.

Mode	Global d_{JS}	d (prism, meta)	d (gratings, meta)
A1 (mean, $N = 253$)	0.1852	0.0949	0.0918
A2 (geo, $\alpha = 10^{-6}$, $N = 253$)	0.4872	0.2994	0.2121

The A1 global distance (0.1852 nats) is substantially smaller than the per-source mean (0.3108 nats), showing the smoothing effect of arithmetic aggregation: source-level fluctuations partially cancel and the global state retains the dominant shared line-ratio structure. The near-equal distances to the midpoint indicate that the two modes are globally almost symmetric under A1. The A2 global distance (0.4872 nats) is much larger. This reflects the overlap-selective character of the geometric estimator: bins in which one mode assigns consistently low weight are suppressed, so persistent inter-mode discrepancies accumulate across sources. The asymmetry in the distances to the midpoint (0.2994 vs. 0.2121) indicates that PRISM departs more from the global geometric consensus than GRATINGS, consistent with the broader line redistribution expected from PRISM's lower spectral resolution. Taken together, A1 and A2 illustrate the estimator distinction emphasized in Section 2.4: A1 provides a linear compromise, whereas A2 sharpens structural disagreement by privileging shared flux concentration.

Null test. At the global level, using Definition 4 with $B = 5000$ surrogates, the A2 observed distance is $d_{\text{JS}}^{\text{obs}} = 0.4925$, whereas the null expectation is $\langle d_{\text{JS}} \rangle_{\text{null}} = 0.5638 \pm 0.0003$ nats, corresponding to $z = -246.64$ and $p_{\text{two}} \approx 4 \times 10^{-4}$. The global PRISM-GRATINGS geometry is therefore more clustered than expected under random bin permutations, showing that the observed inter-mode structure is not a normalization artifact.

6.4. Information-Geometric Structure: Distance Matrix and Stability

To examine the full information-geometric organization beyond global summaries, **Figure 11** shows the pairwise JS distance matrix across all normalized line-flux distributions (PRISM and GRATINGS jointly). The non-random block organization indicates that PRISM sources cluster more tightly among themselves than with GRATINGS sources, consistent with systematic mode-dependent differences in line-flux ratios (**Figure 12**).

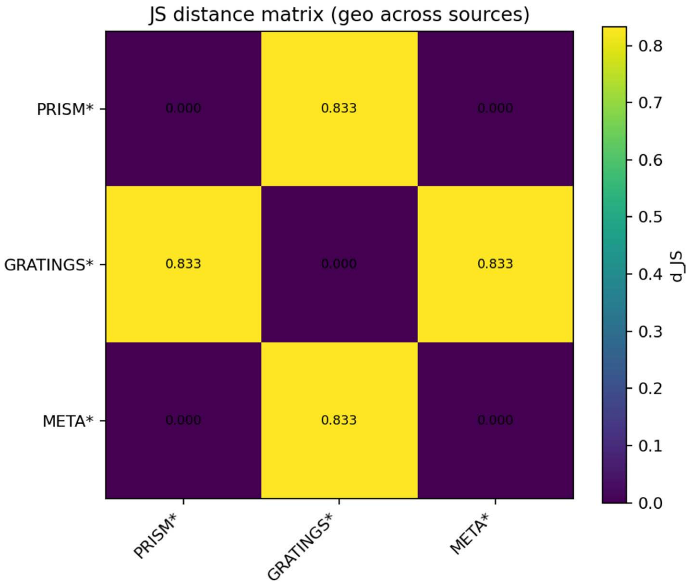

Figure 11. JWST JADES: Jensen-Shannon distance matrix for PRISM and GRATINGS line-flux distributions.

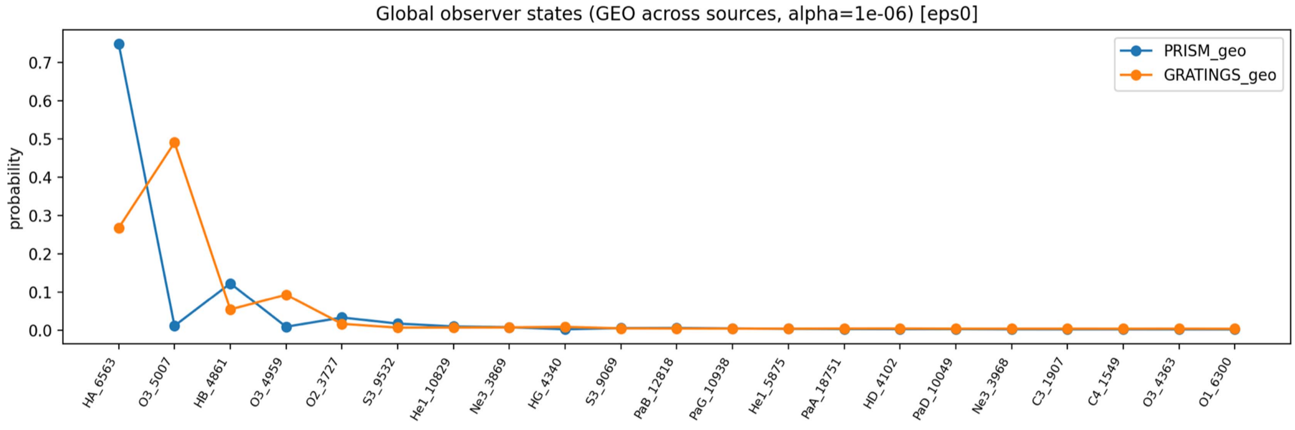

Figure 12. JWST JADES: top-30 line-weight overlay under A2 (geometric) aggregation.

6.5. Position of JWST in the Cross-Domain Hierarchy

The JWST line-flux analysis places the astrophysical domain at the high-dispersion end of the cross-domain distinguishability hierarchy. Its global distances (A1: 0.185 nats; A2: 0.487 nats) substantially exceed the CMB (~10^{-3} nats) and HRV

(~10^{-2} - 10^{-1} nats) values reported in Section 7. This is consistent with the ordering established in [7]: high-resolution astrophysical spectra with multimodal line structure occupy the high-curvature end of JS geometry. Within the present multi-observer framework, the PRISM-GRATINGS pair is the most spectrally heterogeneous observer ensemble among the domains considered here, which explains the large observed dispersion.

7. Empirical Instantiations IV: Large-Scale Structure (LSS)

Large-scale structure data are analyzed within the same information-geometric framework. The purpose is to assess stabilization and cross-sample consistency in the probability simplex, not to introduce alternative cosmological modeling. Two complementary representations are considered: redshift-space $p(z)$ distributions (Part A) and Fourier-space $p(k)$ distributions derived from published power-spectrum monopoles (Part B). Because the two carry different assumption loads, they are expected to exhibit different levels of cross-observer distinguishability: $p(z)$ encodes galaxy-population differences between redshift slices, whereas $p(k)$ averages over angular structure and should therefore be more homogeneous across sub-samples. Within the IFR framework, the hierarchy —large d_{JS} in $p(z)$, small d_{JS} in $p(k)$ —is thus a structural prediction rather than an anomaly.

7.1. Part A: Redshift-Space Geometry (BOSS DR12 $p(z)$)

Data and observer construction. We use weighted redshift distributions $p(z)$ from the BOSS DR12 galaxy catalogs (CMASS/LOWZ × North/South Galactic Cap). Each catalog-cap combination defines an observer-specific distribution on a common redshift grid ($z \in [0,1.2]$, 300 bins). Standard BOSS combined weights are applied:

$$w^{(s)} = w_{\mathrm{FKP}} \cdot w_{\mathrm{SYSTOT}} \cdot w_{\mathrm{CP}} \cdot w_{\mathrm{NOZ}}, \tag{29}$$

and the weighted histogram is normalized to $p^{(s)}(z_k) \geq 0$, $\sum_k p^{(s)}(z_k) = 1$.

Results. Pairwise Jensen-Shannon distances between the four BOSS observers are reported in Table 11 and illustrated in Figure 13 and Figure 14.

Table 11. BOSS DR12 LSS: pairwise Jensen-Shannon distances between $p(z)$ observers (natural log base). Within-sample (NGC vs SGC) distances are small; cross-sample (CMASS vs LOWZ) distances are large, reflecting genuine redshift-slice separation.

Observer pair	d_{JS} (nats)
CMASS NGC vs CMASS SGC	0.039
LOWZ NGC vs LOWZ SGC	0.037
CMASS NGC vs LOWZ NGC	≈0.63
CMASS SGC vs LOWZ SGC	≈0.63
CMASS NGC vs LOWZ SGC	≈0.63
CMASS SGC vs LOWZ NGC	≈0.63

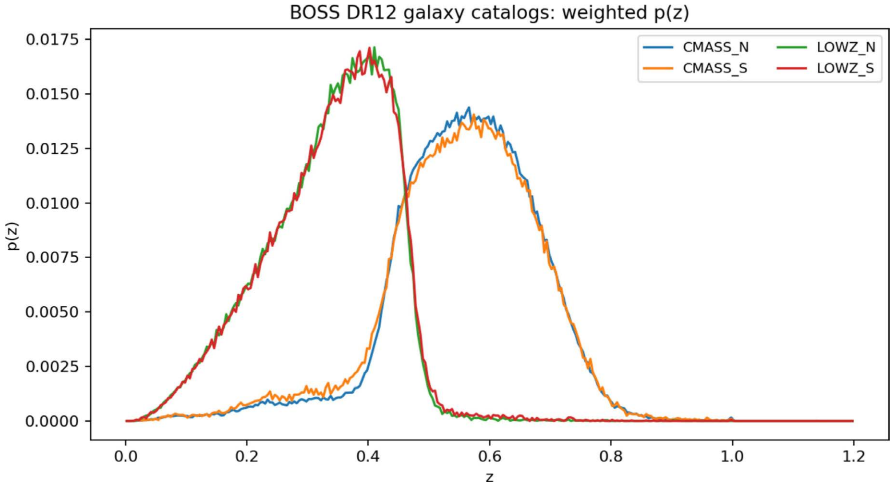

Figure 13. BOSS DR12 LSS: normalized redshift distributions $p(z)$ for CMASS and LOWZ in the north and south galactic caps.

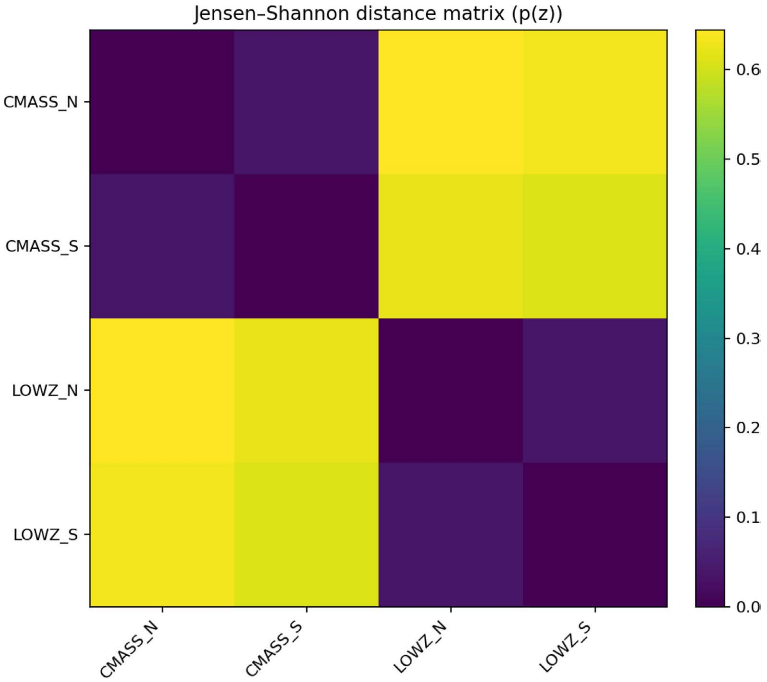

Figure 14. Pairwise Jensen-Shannon distance heatmap for the four BOSS DR12 $p(z)$ observers.

Two features are immediate. First, within-sample distances (NGC vs SGC) are small (≈0.038 nats), showing that the North/South split introduces little informational disagreement: the two sky regions encode the same redshift population. Second, the CMASS-LOWZ separation is large (≈0.63 nats), reflecting the fact that the two samples occupy largely distinct redshift ranges. In this setting, a large JS distance is not a failure of the framework but the expected signature of minimal informational overlap between cosmologically distinct populations.

Aggregation robustness. The observed $p(z)$ geometry is robust with respect to the choice of aggregation rule. In particular, the same block structure is obtained under both arithmetic and geometric embeddings, showing that the main conclusion does not depend on the estimator. For brevity, only the arithmetic heatmap is shown in the main text.

Null test. Applying Definition 4 with $B = 5000$ surrogate realizations, the observed mean pairwise distance between the four redshift distributions is $\bar{d}_{\mathrm{JS}}^{\mathrm{obs}} = 0.431$, while the permutation baseline gives $\langle d_{\mathrm{JS}} \rangle_{\mathrm{null}} = 0.651 \pm 0.007$, corresponding to $z = -29.8$ and $p_{\mathrm{two}} \approx 4 \times 10^{-4}$. The observed geometry therefore reflects genuine within-population coherence between north and south subsamples rather than random bin alignment.

7.2. Part B: Fourier-Space Geometry (BOSS DR12 $p(k)$)

Data and observer construction. We next consider the power-spectrum domain using published BOSS DR12 monopole measurements $P_0(k)$ (public data, multiple redshift bins and Galactic caps). Each (cap, *z*-bin) combination defines an observer-specific distribution $p(k)$ on a common k-grid ($k \in [0.02, 0.30]\,\mathrm{h} \cdot \mathrm{Mpc}^{-1}$, $N_k = 300$ bins, pre-reconstruction):

$$p_i(k_j) = \frac{\max\left(P_0^{(i)}(k_j), 0\right)}{\sum_j \max\left(P_0^{(i)}(k_j), 0\right)}. \tag{30}$$

Results. Pairwise JS distances between $p(k)$ observers are reported in Table 12 and illustrated in Figure 15.

Table 12. BOSS DR12 LSS: characteristic Jensen-Shannon distances between pre-reconstruction $p(k)$ observers. The very small values (~10^{-4} nats) indicate a tightly clustered configuration in JS geometry.

Observer pair	d_{JS} (nats)
Within-cap, adjacent *z*-bins	8.6×10^{-5}
Cross-cap, same *z*-bin	1.68×10^{-4}
Cross-cap, adjacent *z*-bins	1.75×10^{-4}
Global MEAN dispersion $V_N(\bar{p})$	1.02×10^{-4}
Global GEO-estimator dispersion $V_N(p^{\mathrm{G}})$	1.02×10^{-4}

The $p(k)$ distances are many orders of magnitude smaller than the CMASS-LOWZ separations seen in $p(z)$, exactly as predicted. Power-spectrum shapes vary smoothly across redshift bins and Galactic caps, and all observers retain the same broad large-scale structure signature, including the BAO feature around $k \approx 0.06$ - $0.08\,\mathrm{h} \cdot \mathrm{Mpc}^{-1}$. In JS geometry, the corresponding observer ensemble is therefore extremely tightly clustered.

Null test. Using Definition 4 with $B = 5000$ surrogate realizations, the observed mean pairwise distance is $\bar{d}_{\mathrm{JS}}^{\mathrm{obs}} = 1.57 \times 10^{-4}$, whereas the null baseline gives $\langle d_{\mathrm{JS}} \rangle_{\mathrm{null}} = 0.1943 \pm 0.0014$ nats, yielding $z = -136.1$ and $p_{\mathrm{two}} \approx 4 \times 10^{-4}$. The near-overlap of the $p(k)$ observers therefore reflects genuine large-scale structure coherence across BOSS subsamples rather than a normalization artifact.

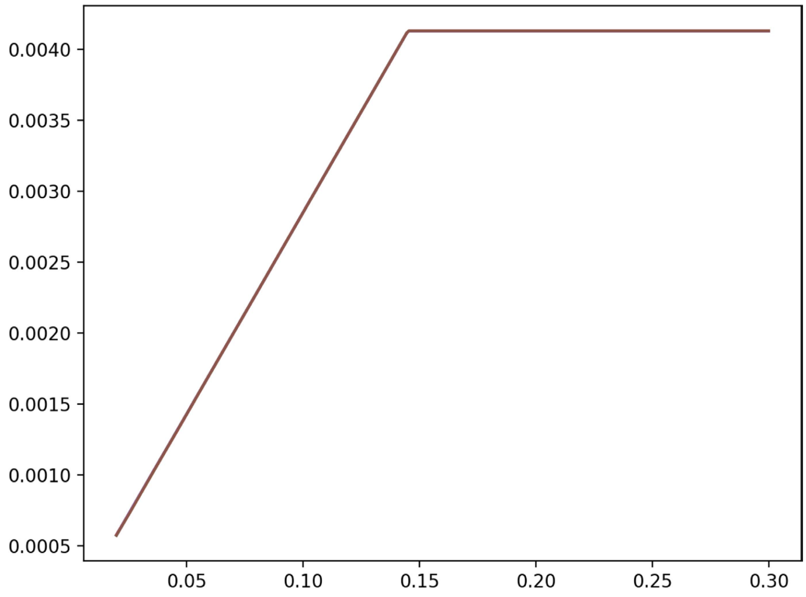

Figure 15. BOSS DR12 $p(k)$ observers on a common pre-reconstruction k-grid.

7.3. Cross-Representation Consistency

The joint $p(z)$ - $p(k)$ analysis yields a two-layer consistency picture with different assumption loads, as summarized in Table 13.

Table 13. BOSS DR12 LSS: cross-representation information-geometric summary. The large $p(z)$ cross-sample distance and the small $p(k)$ cross-sample distance reflect different levels of informational overlap between redshift-sliced and Fourier-integrated representations.

Representation	Comparison	d_{JS} (nats)	Interpretation
$p(z)$	Within-sample (NGC vs SGC)	0.038	Redundant sky-area observers
$p(z)$	Cross-sample (CMASS vs LOWZ)	0.63	Non-overlapping redshift slices
$p(k)$	Within/cross-cap	1.7×10^{-4}	Shared BAO structure
$p(k)$	Cross-z-bin	1.8×10^{-4}	Smooth $P_0(k)$ variation

The contrast between the two representations is itself informative. The $p(z)$ within-sample distances place the BOSS NGC/SGC pairs among the most internally consistent observer ensembles in the paper, whereas the large CMASS-LOWZ distances reflect genuinely distinct redshift populations. By contrast, the uniformly tiny $p(k)$ distances show that once the data are projected into Fourier space, the subsamples become highly homogeneous in information geometry.

The two representations therefore tell a consistent story: large separation where the observational slicing is physically distinct, and near-overlap where the summary representation integrates over the same large-scale structure signal.

8. Cross-Domain Informational Stability

The five empirical domains analyzed in Sections 3-7 span roughly four orders of magnitude in Jensen-Shannon distance and represent physically heterogeneous observational contexts: gravitational-wave strain spectra, cosmological angular power spectra, physiological heart-rate variability, astrophysical emission-line fluxes, and galaxy redshift/power-spectrum distributions. This section consolidates the cross-domain picture, assesses the robustness of the resulting distinguishability hierarchy, and briefly connects it to the emergent-time construction of Section 2.8.

8.1. Distinguishability Hierarchy

Table 14 collects the representative Jensen-Shannon distances for the five domains, ordered by increasing distinguishability.

Table 14. Cross-domain Jensen-Shannon distance summary (natural log base). Representative values are the primary multi-observer distances reported in each empirical section. The hierarchy spans approximately four orders of magnitude, from the most internally consistent observers (CMB processing variants) to the most separated (CMASS vs LOWZ redshift slices and GWOSC cross-event geometric estimators).

Domain	Comparison	d_{JS} (nats)	Notes
CMB	TT: $\sigma = 0.5$ vs $\sigma = 1.0$	$\sim 10^{-3}$	Processing variants; lowest dispersion
CMB	TT vs CAMB ΛCDM	0.004	Planck vs theory
LSS $p(k)$	BOSS DR12 cross-cap/bin	1.7×10^{-4}	Fourier-space; structurally near-overlapping
LSS $p(z)$	NGC vs SGC (within-sample)	0.038	Redundant sky-area observers
HRV	Fantasia f1y01, 3G model	0.075	Empirical vs mixture
JWST	PRISM vs GRATINGS (A1 global)	0.185	Inter-mode; arithmetic aggregation
GW	GW150914 H1 vs L1 (30 - 150 Hz)	0.366	Two-detector, same event
JWST	PRISM vs GRATINGS (A2 global)	0.487	Inter-mode; geometric aggregation
LSS $p(z)$	CMASS vs LOWZ	≈0.63	Non-overlapping redshift slices
GW	GW150914 vs GW170817 (cross-event)	0.652	Event-level geometric estimators
GW	GW170817 H1/L1/V1 mean pairwise	0.677	Three-detector, mixed sensitivity

At the qualitative level, the hierarchy is

$$\begin{aligned} \text{CMB} &\ll \text{LSS } p(k) \lesssim \text{LSS } p(z)_{\text{within}} < \text{HRV} \\ &< \text{JWST}_{A1} < \text{GW150914} < \text{JWST}_{A2} \\ &< \text{LSS } p(z)_{\text{cross}} \sim \text{GW}_{\text{cross-event}} \lesssim \text{GW170817}. \end{aligned} \tag{31}$$

The exact ordering of adjacent entries is less important than the overall stratification: low-dispersion domains (CMB, LSS $p(k)$), intermediate domains

(HRV), and high-dispersion domains (JWST and GW), with LSS $p(z)$ occupying both extremes depending on whether one compares redundant sky-area splits or genuinely distinct redshift populations.

8.2. Physical Interpretation of the Hierarchy

The hierarchy in Equation (31) is physically interpretable in domain-specific terms and does not require a unified causal mechanism across domains.

CMB (lowest dispersion). The Planck angular power spectrum is the most internally redundant object in the dataset. Processing variants such as smoothing scale or bin width introduce only negligible disagreement because the acoustic peak structure is highly compressible. Accordingly, the CMB occupies the low-dispersion end of the hierarchy.

LSS $\boldsymbol{p(k)}$ and HRV (low to intermediate). The LSS $p(k)$ representation is likewise highly stable: power-spectrum shapes vary smoothly across BOSS subsamples and retain the same broad BAO structure. HRV lies higher in the hierarchy because physiological spectra reflect finite recording length and subject-dependent variability, even though they remain far more constrained than JWST or GW ensembles.

JWST and GW (high dispersion). JWST PRISM-GRATINGS disagreement reflects mode-dependent redistribution of line weights, while GW intra-event disagreement reflects genuine detector heterogeneity. In both cases the observer channels are structurally less redundant than in CMB or HRV, and the resulting JS distances are correspondingly larger.

LSS $\boldsymbol{p(z)}$ and GW cross-event (maximal separation). The largest distances arise when the compared observers encode genuinely distinct physical content. For LSS $p(z)$ this occurs for CMASS vs LOWZ, which probe different redshift populations. For GW cross-event comparisons, it occurs between GW150914 and GW170817, whose event-level barycenters represent distinct observational contexts. In both cases, a large JS distance is an informative outcome rather than a failure of stabilization.

Remark. Within the IFR operational framework, large d_{JS} does not imply that a domain is "less objective" or "less real". Objectivity is defined by *within-domain* barycenter stability as the number of observers grows (Theorem 1), not by the absolute scale of inter-observer distance. Large cross-event or cross-domain distances simply indicate that the corresponding observational contexts encode different physical content.

8.3. Robustness of the Hierarchy

The cross-domain ordering is robust along three independent axes.

Bootstrap resampling. Bootstrap confidence intervals reported in the empirical sections show that the representative distances are stable under resampling. The hierarchy is therefore not driven by isolated realizations.

Aggregation method. Where both arithmetic and geometric aggregations were computed (notably JWST and LSS), the qualitative ordering is preserved. The geometric estimator typically yields larger distances because it amplifies structural disagreement, but it does not alter the overall cross-domain picture.

Permutation null tests. Permutation-based null tests were performed in all empirical domains using Definition 4. In every case, the observed distances lie well below the corresponding null baselines, often by very large standardized margins. This shows that the reported geometries arise from genuine shared structure in the underlying data rather than from normalization artifacts or random bin alignment.

8.4. Connection to Emergent Time

The cross-domain hierarchy has a natural connection to the emergent-time construction of Equation (15). If successive collective states $p^{*(n)}$ are identified with barycenters computed at successive observational epochs, then the cumulative informational arc-length T_n grows slowly in domains where successive states remain close in JS geometry and more rapidly in domains where successive states are strongly separated.

In this programmatic sense, the hierarchy may be read as a hierarchy of representational rates of informational change: the CMB provides a near-static informational baseline, whereas GW cross-event and LSS $p(z)$ cross-sample comparisons exemplify configurations in which informational arc-length accumulates much more rapidly. A quantitative treatment of this connection, including its relation to physical time parameters in each domain, is deferred to the companion study.

9. Empirical Validation of the Stabilization Principle

The interference-first framework makes a definite structural prediction: under redundant observation, the Jensen-Shannon barycenter of observer-induced probability distributions becomes increasingly stable, and, in favorable multi-observer settings, its total dispersion under $\mathcal{V}_N$ (Equation (12)) may contract relative to linear aggregation as the observer family becomes richer. This section summarizes the extent to which the empirical results of Sections 3-7 support that prediction, while clarifying the present scope of the validation.

9.1. Metric Specificity and Empirical Support

The stabilization analysis is not metric-arbitrary. As established in Section 2.3, the Jensen-Shannon metric is bounded, symmetric, satisfies the triangle inequality, and is compatible with the geometry of the probability simplex [10]. These properties ensure that Fréchet means are well-defined on Δ°, that the dispersion functional $\mathcal{V}_N$ is continuous and admits minimizers, and that Theorem 1 provides the direct reference case for the geometry used here. The reported stabilization results are therefore specific to Jensen-Shannon geometry and should not be read as metric-independent statements.

Empirically, the cross-domain analyses establish a clear pattern. Within each domain, physically aligned observers are systematically closer to one another than structurally distinct observers. Examples include BOSS NGC vs SGC (0.038 nats) versus CMASS vs LOWZ (≈0.63 nats), and GW intra-event geometry versus GW cross-event geometry. Low-dispersion domains such as CMB and LSS $p(k)$ correspond to highly redundant observational summaries, whereas higher-dispersion domains such as JWST and GW involve structurally heterogeneous observer channels. In this sense, the empirical material supports the core qualitative prediction of Theorem 1: redundancy drives clustering toward a shared barycentric state.

9.2. Multi-Observer Contraction and Present Scope

In what follows, *contraction* is used in one strict and uniform sense only: $\rho < 1$, where ρ compares the total dispersion of the geometric overlap estimator p^{G} with that of the arithmetic mean under the common functional $\mathcal{V}_N$. A more direct quantitative test of stabilization is the comparison between the geometric overlap estimator p^{G} and the arithmetic mean $\bar{p}$ through the dispersion functional $\mathcal{V}_N$ of Equation (12). When both estimators are available, one may compare their total disagreement by means of the ratio

$$\rho = \mathcal{V}_N\left(p^{\mathrm{G}}\right) / \mathcal{V}_N\left(\bar{p}\right). \tag{32}$$

Values below 1 indicate that the geometric overlap estimator achieves lower total JS dispersion than the arithmetic mean, while values above 1 indicate the opposite. Table 15 summarizes the corresponding results for the domains in which both estimators were explicitly evaluated.

Table 15. Multi-observer contraction: ratio of geometric-estimator dispersion to arithmetic-mean dispersion, $\rho = \mathcal{V}_N\left(p^{\mathrm{G}}\right) / \mathcal{V}_N\left(\bar{p}\right)$. Values below 1 indicate lower total disagreement for the geometric estimator under the JS dispersion functional.

Domain	Setting	$\mathcal{V}_N\left(p^{\mathrm{G}}\right)$	$\mathcal{V}_N\left(\bar{p}\right)$	ρ
GW150914	$N = 2$ (H1, L1)	0.1921	0.1901	1.010
GW150914	$N = 6$ multiband	0.0861	0.0804	1.071
GW170817	$N = 3$ (H1, L1, V1)	0.2986	0.3083	0.969
JWST	A1 global Comparison ($N = 253$)	0.1852	0.1852	1.000
LSS $p(z)$	$N = 4$ (CMASS/LOWZ)	0.4217	0.4311	0.978

For JWST, the A1 row is included only as a linear-symmetry baseline for comparison; it should not be read as a separate contraction result of the same type as the genuinely multi-observer GW and LSS cases.

The results show that contraction in the strict sense $\rho < 1$ is present in some genuinely multi-observer settings, most clearly for GW170817 and LSS $p(z)$. These cases support the idea that geometric aggregation can reduce collective disagreement when the observer family is sufficiently heterogeneous and genuinely multi-member.

At the same time, the present dataset also shows that geometric stabilization and strict contraction should not be conflated. In particular, the GW150914 multiband case ($N = 6$) does *not* satisfy $\rho < 1$ under the dispersion functional of Equation (12): for that ensemble, the arithmetic mean yields a slightly lower total JS dispersion than the geometric overlap estimator. Its empirical relevance therefore lies elsewhere, namely in the stability of the collective geometric summary under observer enrichment and in the progressive peripheral displacement of broadband reconstructions in the emergent simplex.

For $N = 2$, by contrast, the arithmetic and geometric estimators are expected to remain close. This is exactly what is observed in the original GW150914 two-detector case, where the two constructions are nearly indistinguishable at the level of total dispersion.

Remark. For $N = 2$ with uniform weights, the arithmetic mean is already a near-minimizer of the relevant JS dispersion functional, so little separation from the geometric estimator should be expected. The overlap-selective advantage of the geometric overlap estimator becomes more informative for $N \geq 3$ and for ensembles with heterogeneous spectral shapes, where discrepant bins can be down-weighted more aggressively than under linear averaging. Accordingly, the GWOSC multiband case should be read as evidence of collective geometric stabilization rather than as a strict contraction example in the sense of Table 15.

The clearest explicit N-dependence currently available in the present dataset is therefore not a monotonic decrease of $\mathcal{V}_N$ in every enriched ensemble, but the growing interpretive value of the geometric estimator as the observer family becomes genuinely multi-member and spectrally heterogeneous. In the GWOSC multiband transition ($N = 2 \to 6$), the barycenter remains stable as additional observers are added and broadband reconstructions move toward the periphery of the simplex, even though the arithmetic mean retains a slightly lower JS dispersion in the strict sense of Equation (12).

At the same time, the present validation has a clear limit: the current analyses establish collective geometric stabilization, but not yet the sequential within-domain trajectories required for a direct empirical test of emergent time. That extension is deferred to future work.

10. Discussion

10.1. Emergence of Objectivity from Redundancy

A central implication of the IFR framework is that physical objectivity does not require either a privileged observer or a pre-given classical domain. Rather, it emerges as a collective and asymptotic effect of redundancy among independent observational records. Each observer induces a valid but partial representation of an underlying interference structure, yielding a probability distribution in the interior of the probability simplex. As the number of independent observations increases, the dispersion among these representations contracts and their Jensen-Shannon barycenter stabilizes, as stated in Theorem 1 and supported by the cross-domain analyses of the present work.

Objectivity is therefore identified not with any single record, but with the stable collective state

$$p^{\mathrm{F}} = \mathcal{S}\left(\left\{p_i\right\}\right),$$

which remains approximately invariant under further redundant interrogation. In this sense, IFR is conceptually related to decoherence theory [12] and to quantum Darwinism [11], both of which link classical stability to redundancy. The difference is that IFR operates entirely at the level of probability representations: no Hilbert space, quantum state, or specific decoherence mechanism is assumed. Objectivity is identified instead with a geometric invariant—the Fréchet barycenter in the Jensen-Shannon metric. The relation to quantum Darwinism is therefore structural and interpretive rather than derivational.

10.2. Holographic Substrate and Probability Simplex

The interference substrate $\Phi \in \mathcal{H}$ and the probability simplex Δ° belong to distinct levels of description. The substrate is pre-observational and non-statistical: it does not itself encode probabilities, outcomes, or classical observables. The simplex appears only after observer-induced projection and normalization,

$$\Pi_O\left(\Phi\right) = p_O \in \Delta^{\circ},$$

and provides the representational space in which observable alternatives can be compared, aggregated, and geometrically organized.

This distinction clarifies the status of probability in the IFR framework. Probability distributions are not fundamental entities, but stabilized projections of an underlying interference structure. The metric structure induced by d_{JS} therefore does not describe the substrate directly; it describes the geometry of observer-accessible representations.

The capacity bound of Equation (18),

$$H\left(p^{(N)}\right) \le \mathcal{C},$$

suggests a structural analogy with holographic entropy arguments [1] [2] [4]: the operational degrees of freedom accessible to an observer ensemble are bounded, and stabilization can be read as the approach of the collective state toward an effective observational boundary. At present, this should be understood as an analogy and a direction for future formalization, not as a derived holographic theorem.

10.3. Relation to Holographic and Boundary-Based Descriptions

Modern holographic approaches, including AdS/CFT [5] and celestial holography [22] [23], emphasize that physical information may be more naturally encoded in boundary-like descriptions than in localized bulk variables. The IFR framework shares this general intuition, but differs in a crucial respect: it does not take spacetime, asymptotic structure, or boundary geometry as primitive.

In IFR, the relevant "boundary" is informational rather than spatial. Spacetime and classical structure enter only at the level of stabilized observational representation. In this limited sense, the framework may be read as a more abstract form of holographic reasoning, in which stabilization replaces asymptotic symmetry as the organizing principle. Whether this analogy can be developed quantitatively remains open.

10.4. Observer-Independence and Operational Realism

The IFR framework also bears on the long-standing concern that physical reality should not depend on any single observer. Within the interference-first picture, this concern is addressed without returning to classical determinism.

A pre-observational interference substrate may exist independently of any individual observer, but it is not yet physical reality in the operational sense relevant to measurement. Reality emerges only through projection, normalization, and collective stabilization. No single observation creates reality; rather, reality is identified with what remains invariant under many independent observations. This motivates a geometric form of operational realism: what is physically real is what is stable under redundant informational constraints.

10.5. Toward a Minimal Formal Scaffold

The present framework suggests a minimal formal scaffold organized around three primitive operations:

1) an interference substrate $\mathcal{I}$ with $\Phi \in \mathcal{I}$;

2) a manifestation map $\Pi : \mathcal{I} \to \Delta^{\circ}$ producing observer-induced probability distributions;

3) a stabilization operator $\mathcal{S}$ producing collective invariants.

In compact form,

$$\Pi(\Phi) = p \in \Delta^{\circ}, \quad \mathcal{S}\left(\{p_i\}_{i=1}^{N}\right) = p^{F}, \tag{33}$$

with

$$p^{\mathrm{F}} = \arg\min_{p \in \Delta^{\circ}} \sum_i d_{\mathrm{JS}}^2 (p_i, p).$$

Within this scaffold, the observable collective state p^{F} contains... Collective dynamics may then be represented, at the programmatic level, as a trajectory of successive collective states

$$\gamma(n) = p_{\mathrm{coll}}^{(n)} \in \Delta^{\circ},$$

with emergent time identified with the cumulative Jensen-Shannon arc-length of Equation (15). Objectivity corresponds to convergence toward geometric invariance; temporal asymmetry corresponds to cumulative informational displacement.

A complete interference-based formalism in which $\mathcal{I}$, Π, and $\mathcal{S}$ are primitive and spacetime or Hilbert-space structure are derived remains an open program. The present paper does not complete that program. What it does provide is a concrete information-geometric basis for it: the metric space $\left(\Delta^{\circ}, d_{\mathrm{JS}}\right)$, the stabilization theorem (Theorem 1), the null-test protocol (Definition 4), and reproducible empirical instantiations across five independent physical domains.

10.6. Predictive Consequences of Stabilization Geometry

The geometric interpretation of multi-observer stabilization also suggests several quantitative consequences that can be tested more directly in future work.

First, if observer-induced distributions are independent samples from a common underlying generative process, then standard concentration results for Fréchet means on metric spaces suggest that dispersion around the collective barycenter should decrease with the number of observers approximately as

$$\sigma_N \propto N^{-1/2}.$$

Within the present framework this should be understood as an *expected scaling under standard concentration assumptions*, not as an empirical law established by the current dataset. A systematic multi-domain N-sweep would be required to test this prediction quantitatively.

Second, because Jensen-Shannon geometry is bounded and symmetric, barycentric structure should remain stable under moderate smoothing or regularization of the underlying probability distributions. The empirical robustness observed across aggregation choices and regularized constructions is consistent with this expectation.

Third, if the stabilization mechanism is genuinely representation-level rather than domain-specific, then analogous information-geometric organization should reappear across heterogeneous empirical contexts once their measurements are mapped to normalized probability representations. The analyses of CMB, HRV, JWST spectroscopy, large-scale structure, and gravitational-wave observations provide initial support for this possibility.

Taken together, these considerations suggest that objectivity may be interpreted as a concentration phenomenon in information space rather than as a primitive property of physical systems.

11. Scope and Limitations

The present framework is representational and information-geometric. It does not provide a microscopic derivation of the interference substrate, does not replace standard quantum-mechanical or field-theoretic descriptions, and does not predict new physical interactions. All claims concerning objectivity and reality are therefore operational: they concern stabilization properties in the probability simplex under multi-observer aggregation.

Cross-domain comparisons should likewise be interpreted as structural consistencies within a common information-geometric representation, not as evidence of shared microscopic mechanisms. Their value lies in showing that redundancy-driven stabilization can be formulated and tested across physically heterogeneous domains within a single bounded metric geometry.

Several limitations should be stated explicitly. More fundamentally, the interference substrate Φ and its internal structure are not directly observable: the empirical analyses test only the induced probability distributions $\{p_i\}$ and their Jensen-Shannon geometry. Claims about the substrate should therefore be read as ontological scaffolding rather than as directly validated empirical statements.

The emergent-time construction also remains programmatic. Because $d_{\text{JS}} \geq 0$, the cumulative informational displacement

$$T_n = \sum_{k=1}^{n} d_{\text{JS}}\left(p^{*(k)}, p^{*(k-1)}\right)$$

defines a mathematically coherent, monotonically non-decreasing arc-length in the probability simplex. This gives the framework a formal notion of temporal asymmetry at the level of collective representation: time reversal would require reversing the underlying assimilation dynamics rather than merely inverting the arc-length parameter. A direct relation between this informational arc-length and physical time, however, requires ordered within-domain sequences of stabilized collective states indexed by epoch, redshift slice, frequency band, or an analogous observational parameter. No such sequential within-domain analysis has been carried out here, and establishing that relation is deferred explicitly to the companion study.

Finally, the novelty of the present framework should be stated precisely. Theorem 1 is an application of standard Fréchet mean consistency in a bounded metric space [14]. Its novelty lies not in the abstract mathematical result itself, but in the identification of the Jensen-Shannon metric as a natural geometry for multi-observer aggregation, together with its empirical instantiation across physically distinct domains. Likewise, the relation to quantum Darwinism is complementary rather than competitive: IFR does not derive or replace it, but provides a Hilbert-space-free description of redundancy-driven objectivity.

12. Conclusions

We have developed the Interference-First Reality (IFR) framework, in which physical objectivity is defined operationally through the geometric stabilization of observer-induced probability distributions in the Jensen-Shannon metric on the probability simplex.

On the theoretical side, we formalized a multi-observer setting in which objectivity is identified with the stabilization of empirical Fréchet means (Theorem 1), provided a complete proof of barycenter consistency, introduced a complementary geometric estimator based on Dirichlet-regularized overlap, and defined a permutation-based null-test protocol (Definition 4) for assessing the non-triviality of the inferred geometry.

On the empirical side, the framework was instantiated across five independent physical domains: cosmological microwave background (CMB), heart-rate variability (HRV), JWST astronomical spectroscopy, large-scale structure (LSS), and gravitational-wave open data (GWOSC). Across these domains, we obtained reproducible multi-observer barycentric summaries, bounded Jensen-Shannon distances consistent with the stabilization picture, and a cross-domain distinguishability hierarchy spanning approximately four orders of magnitude. Within each domain, physically redundant observers cluster near a shared barycenter, whereas structurally discrepant observers lie farther from the collective center, in agreement with Theorem 1.

The resulting hierarchy is stable under bootstrap resampling and, where tested, under variation of the aggregation rule. Its interpretation is domain-specific rather than universal: it reflects differences in observational redundancy, structural heterogeneity, and spectral compressibility across the analyzed datasets. Two scope conditions deserve emphasis. First, the GW150914/GW170817 cross-event comparison is informative at the level of observer-ensemble geometry, but in the present form it should be interpreted mainly as a comparison of observational contexts, detector configurations, and noise-weighted spectral representations rather than as a direct measure of intrinsic event-to-event physics. Second, the JWST case probes structured instrumental heterogeneity—most notably PRISM versus GRATINGS channels within a common survey context—and therefore tests multi-observer stabilization under heterogeneous acquisition modes rather than across fully independent observing platforms.

The emergent-time construction—in which time is defined as cumulative Jensen-Shannon arc-length between successive stabilized collective states—remains programmatic in the present work. No within-domain sequential analysis has been carried out here, and the relation between the information-geometric arc-length T_n and physical time in any specific domain is left to a companion study.

The IFR framework does not propose new physical interactions, nor does it modify established quantum-mechanical or relativistic descriptions. Its contribution is to introduce a geometric layer of description at the level of observer-induced probability representations, grounded in standard metric barycenter theory and tested across multiple public-domain empirical settings.

Whether the geometric structures identified here will ultimately prove foundationally significant—for example in relation to dynamical emergence, holographic constraints, or relational formulations of quantum theory—remains open. The present work is intended as a concrete information-geometric foundation for that broader program, together with a reproducible empirical basis for pursuing it further.

Author Contributions

Conceptualization, M.B.; methodology, M.B.; software, M.B.; validation, M.B.; formal analysis, M.B.; visualization, M.B.; writing—original draft preparation, M.B.; writing—review and editing, M.B.

Data Availability

All datasets used in this study are publicly available. CMB spectra (TT, TE, EE) are from the Planck 2018 legacy release (Planck Legacy Archive) [16]; for theoretical background on CMB anisotropies see [24] [25]. Scripts associated with the legacy CMB and HRV analyses are archived separately in the Zenodo repository accompanying the previous article. https://zenodo.org/records/17672528.

Gravitational-wave strain data (GW150914-v2 and GW170817-v2) are from the Gravitational Wave Open Science Center (GWOSC). ECG/HRV records are from PhysioNet (*Fantasia* and *MIT-BIH Arrhythmia* databases); PSD was estimated using the Welch method [15] and frequency-band definitions follow established HRV standards [18]. No raw ECG signals are redistributed. JWST spectroscopic data are from the public JADES release [21]. All datasets, Python scripts, and LaTeX materials are openly available on Zenodo at https://zenodo.org/records/19023679.

Generative AI Tools

Generative AI tools (Claude by Anthropic, and GPT-based assistants) were used for manuscript revision, LaTeX formatting, code refactoring, and minor stylistic editing. All analyses, parameter choices, and numerical results were obtained by executing the released Python code on public datasets. Apart from **Figure 1**, which was generated with ChatGPT as a conceptual illustration, no data, numerical results, or scientific conclusions were generated by AI tools; all scientific analyses, interpretations, and conclusions are the author's own.

Reproducibility and Computational Transparency

All commands, input specifications, execution order, and output descriptions required to fully reproduce the analyses presented in this work are provided in the supplementary file *Reproducibility_sequence.txt*. This document contains the complete pipeline description covering all five domains (HRV, CMB, GWOSC, JWST, LSS, and cross-domain synthesis), including both computational pathways for the CMB section (binned-direct and bootstrap + sweep) and the detailed sequence used to generate every figure and table in the paper.

Acknowledgements

The author thanks the editorial team of JAMP for their professional handling of previous submissions, and acknowledges managing editor *Nancy Ho* for her commitment to high publication standards. The author also thanks the Planck Legacy Archive, GWOSC, JWST/JADES, and PhysioNet teams for maintaining open-access scientific data repositories that made the cross-domain analyses in this work possible.

Conflicts of Interest

The author declares no conflicts of interest regarding the publication of this paper.

References

[1] Bekenstein, J.D. (1973) Black Holes and Entropy. *Physical Review D*, **7**, 2333-2346. https://doi.org/10.1103/physrevd.7.2333

[2] ‘t Hooft, G. (1993) Dimensional Reduction in Quantum Gravity, Salamfestschrift: A Collection of Talks. World Scientific.

[3] Susskind, L. (1995) The World as a Hologram. *Journal of Mathematical Physics*, **36**, 6377-6396. https://doi.org/10.1063/1.531249

[4] Bousso, R. (2002) The Holographic Principle. *Reviews of Modern Physics*, **74**, 825-874. https://doi.org/10.1103/revmodphys.74.825

[5] Maldacena, J. (1998) The Large N Limit of Superconformal Field Theories and Supergravity. *Advances in Theoretical and Mathematical Physics*, **2**, 231-252. https://doi.org/10.4310/atmp.1998.v2.n2.a1

[6] Bianchi, M. (2025) Quantum Holographic Consciousness Theory (QHCT): A Lagrangian Formulation of an Interference-First Holographic Framework and Planck-Oriented Validation. *NeuroQuantology*, **23**, 166-187.

[7] Bianchi, M. (2025) Information Geometry, Coherence, and the Emergence of Time: A Cross-Domain Analysis from Cosmology to Physiology. *Journal of Applied Mathematics and Physics*, **13**, 4355-4378. https://doi.org/10.4236/jamp.2025.1312240

[8] Shannon, C.E. (1948) A Mathematical Theory of Communication. *Bell System Technical Journal*, **27**, 623-656. https://doi.org/10.1002/j.1538-7305.1948.tb00917.x

[9] Lin, J. (1991) Divergence Measures Based on the Shannon Entropy. *IEEE Transactions on Information Theory*, **37**, 145-151. https://doi.org/10.1109/18.61115

[10] Amari, S. and Nagaoka, H. (2000/2016) Methods of Information Geometry. American Mathematical Society, Translations of Mathematical Monographs, 191.

[11] Zurek, W.H. (2009) Quantum Darwinism. *Nature Physics*, **5**, 181-188. https://doi.org/10.1038/nphys1202

[12] Zeh, H.D. (1970) On the Interpretation of Measurement in Quantum Theory. *Foundations of Physics*, **1**, 69-76. https://doi.org/10.1007/bf00708656

[13] Fréchet, M. (1948) Les Éléments Aléatoires de Nature Quelconque dans un Espace Distancié. *Annales de l’Institut Henri Poincaré*, **10**, 215-310.

[14] Sturm, K.-T. (2003) Probability Measures on Metric Spaces of Nonpositive Curvature. In: Auscher, P., *et al.*, Eds., *Heat Kernels and Analysis on Manifolds*, *Graphs*, *and Metric Spaces*, American Mathematical Society, Contemporary Mathematics, Vol. 338, 357-390.

[15] Welch, P.D. (1967) The Use of Fast Fourier Transform for the Estimation of Power Spectra: A Method Based on Time Averaging over Short, Modified Periodograms. *IEEE Transactions on Audio and Electroacoustics*, **15**, 70-73. https://doi.org/10.1109/tau.1967.1161901

[16] Alves, J., Forveille, T., Pentericci, L. and Shore, S. (2020) *Planck* 2018 Results. *Astronomy & Astrophysics*, **641**, E1. https://doi.org/10.1051/0004-6361/202039265

[17] Goldberger, A.L., Amaral, L.A.N., Glass, L., Hausdorff, J.M., Ivanov, P.C., Mark, R.G., *et al.* (2000) PhysioBank, PhysioToolkit, and PhysioNet: Components of a New Research Resource for Complex Physiologic Signals. *Circulation*, **101**, e215-e220. https://doi.org/10.1161/01.cir.101.23.e215

[18] Task Force of the European Society of Cardiology and the North American Society of Pacing and Electrophysiology (1996) Heart Rate Variability: Standards of Measurement, Physiological Interpretation and Clinical Use. *European Heart Journal*, **17**,

354-381.

[19] Torrent-Guasp, F., Buckberg, G.D., Clemente, C., Cox, J.L., Coghlan, H.C. and Gharib, M. (2001) The Structure and Function of the Helical Heart and Its Buttress Wrapping. I. The Normal Macroscopic Structure of the Heart. *Seminars in Thoracic and Cardiovascular Surgery*, **13**, 301-319. https://doi.org/10.1053/stcs.2001.29953

[20] Kocica, M.J., Corno, A.F., Carreras-Costa, F., Ballester-Rodes, M., Moghbel, M.C., Cueva, C.N.C., *et al.* (2006) The Helical Ventricular Myocardial Band: Global, Three-Dimensional, Functional Architecture of the Ventricular Myocardium. *European Journal of Cardio-Thoracic Surgery*, **29**, S21-S40. https://doi.org/10.1016/j.ejcts.2006.03.011

[21] Eisenstein, D.J. (2023) The JWST Advanced Deep Extragalactic Survey (JADES): Overview and First Results. *The Astrophysical Journal Letters*, **957**, L15.

[22] Strominger, A. (2018) Lectures on the Infrared Structure of Gravity and Gauge Theory. Princeton University Press. https://doi.org/10.23943/9781400889853

[23] Pasterski, S., Shao, S.-H. and Strominger, A. (2021) Flat Space Amplitudes and Conformal Symmetry of the Celestial Sphere. *Physical Review D*, **104**, Article ID: 065022.

[24] Hu, W. and Sugiyama, N. (1995) Small-Scale Cosmological Perturbations: An Analytic Approach. *The Astrophysical Journal*, **444**, 489-506.

[25] Hu, W. and Dodelson, S. (2002) Cosmic Microwave Background Anisotropies. *Annual Review of Astronomy and Astrophysics*, **40**, 171-216. https://doi.org/10.1146/annurev.astro.40.060401.093926

[26] Vaart, A.W.v.d. (1998) Asymptotic Statistics. Cambridge University Press. https://doi.org/10.1017/cbo9780511802256

Abbreviations

CMB	Cosmic Microwave Background
GWOSC	Gravitational Wave Open Science Center
HRV	Heart Rate Variability
IFR	Interference-First Reality
JS	Jensen-Shannon divergence
JSD	Jensen-Shannon distance
JWST	James Webb Space Telescope
KL	Kullback-Leibler divergence
LSS	Large-Scale Structure
PSD	Power Spectral Density
VLF/LF/HF	Very-Low/Low/High Frequency bands

Appendix A. Proof of Theorem 1

Proof. We provide a self-contained metric-space proof based on Fréchet mean theory.

Setup. Let $K \in \mathbb{N}$ be fixed and let

$$\bar{\Delta}_K := \left\{ p \in \mathbb{R}^K : p_k \ge 0, \sum\nolimits_{k=1}^{K} p_k = 1 \right\}$$

be the closed probability simplex. Equip $\bar{\Delta}_K$ with the Jensen-Shannon metric $d_{\mathrm{JS}}(p,q) = \sqrt{D_{\mathrm{JS}}(p \,\|\, q)}$. Since D_{JS} is bounded ($D_{\mathrm{JS}} \le \ln 2$ in nats), d_{JS} is bounded and $(\bar{\Delta}_K, d_{\mathrm{JS}})$ is a bounded metric space. Moreover, $\bar{\Delta}_K$ is compact in the Euclidean topology and d_{JS} is continuous on $\bar{\Delta}_K \times \bar{\Delta}_K$, so $(\bar{\Delta}_K, d_{\mathrm{JS}})$ is a compact metric space.

Remark. The theorem is stated for distributions in the interior Δ° (interior-simplex condition, assumption (ii)). The proof extends to the closed simplex $\bar{\Delta}_K$ by compactness; the interior condition ensures that d_{JS} is well-defined and finite for all observer pairs and that $D_{JS}(p_i \,\|\, p)$ is continuous as a function of p on $\bar{\Delta}_K$. In practice, the empirical distributions used throughout the paper satisfy $p_k > 0$ for all k (after projection to a common master grid and Dirichlet smoothing where required), so the interior condition holds for all datasets analyzed.

Step 1: Population Fréchet functional and existence of minimizers. Let P be a $\bar{\Delta}_K$-valued random variable representing an observer-induced probability state. Define the population Fréchet functional

$$F(p) := \mathbb{E}\left[d_{\mathrm{JS}}(P, p)^2 \right] = \mathbb{E}\left[D_{\mathrm{JS}}(P \,\|\, p) \right], \quad p \in \bar{\Delta}_K. \tag{34}$$

Since d_{JS} is bounded, $F(p) < \infty$ for all p. Continuity of d_{JS} implies continuity of $p \mapsto d_{\mathrm{JS}}(x, p)^2$ for each fixed $x \in \bar{\Delta}_K$; dominated convergence then yields continuity of F on $\bar{\Delta}_K$. Since $\bar{\Delta}_K$ is compact and F is continuous, F attains its minimum: there exists at least one population Fréchet mean

$$p^{\infty} \in \arg\min_{p \in \bar{\Delta}_K} F(p). \tag{35}$$

This establishes part (a) of the theorem.

Step 2: Empirical Fréchet functional. Let $\{P_i\}_{i \ge 1}$ be i.i.d. copies of P and let $\{p_i\}_{i=1}^{N}$ denote a realization. For weights $w_{i,N} \ge 0$ with $\sum\nolimits_{i=1}^{N} w_{i,N} = 1$ and $\max_i w_{i,N} \to 0$ as $N \to \infty$ (satisfied in particular by uniform weights $w_{i,N} = 1/N$), define the empirical Fréchet functional

$$F_N(p) := \sum_{i=1}^{N} w_{i,N} d_{\mathrm{JS}}(p_i, p)^2 = \sum_{i=1}^{N} w_{i,N} D_{\mathrm{JS}}(p_i \,\|\, p). \tag{36}$$

The dispersion functional $\mathcal{V}_N$ of Equation (12) coincides with F_N. By the same compactness/continuity argument, F_N attains its minimum on $\bar{\Delta}_K$: there exists at least one empirical Fréchet mean

$$p^{(N)} \in \arg\min_{p \in \bar{\Delta}_K} F_N(p). \tag{37}$$

Step 3: Uniform law of large numbers. For each fixed $p \in \bar{\Delta}_K$, the weighted law of large numbers gives $F_N(p) \to F(p)$ almost surely as $N \to \infty$. Moreover, because $\bar{\Delta}_K$ is compact and $(x, p) \mapsto d_{\mathrm{JS}}(x, p)^2$ is continuous and uniformly bounded on $\bar{\Delta}_K \times \bar{\Delta}_K$, by the uniform law of large numbers for bounded continuous functions on compact spaces [26], the convergence holds uniformly:

$$\sup_{p \in \bar{\Delta}_K} \left| F_N(p) - F(p) \right| \xrightarrow[N \to \infty]{a.s.} 0. \tag{38}$$

Step 4: Argmin consistency (stabilization). Let $\mathcal{M} := \arg\min_{p \in \bar{\Delta}_K} F(p)$ denote the set of population Fréchet means. Uniform convergence (38), combined with compactness of $\bar{\Delta}_K$ and continuity of F, implies argmin-consistency by a standard argument [14] [26]: every sequence $\left\{ p^{(N)} \right\}$ with $p^{(N)} \in \arg\min F_N$ satisfies

$$\operatorname{dist}_{d_{\mathrm{JS}}}\left(p^{(N)}, \mathcal{M} \right) \xrightarrow[N \to \infty]{a.s.} 0. \tag{39}$$

This establishes part (b) of the theorem.

If the population minimizer is unique, $\mathcal{M} = \left\{ p^{\infty} \right\}$, then

$$d_{\mathrm{JS}}\left(p^{(N)}, p^{\infty} \right) \xrightarrow[N \to \infty]{a.s.} 0, \tag{40}$$

which is the barycenter stabilization statement of part (c).

Step 5: Convergence of minimal dispersion. Evaluating (38) at the empirical minimizers yields

$$F_N\left(p^{(N)} \right) \xrightarrow[N \to \infty]{a.s.} \inf_{p \in \bar{\Delta}_K} F(p). \tag{41}$$

While $F_N\left(p^{(N)} \right)$ need not be monotone in N for finite samples, it stabilizes asymptotically: the collective barycenter becomes a geometric invariant of the underlying observer distribution in the large-N regime.

Physical interpretation. Steps 1-5 together establish that, whenever independent observers sample probability distributions from a common population P on the probability simplex with the Jensen-Shannon metric, the empirical Fréchet mean $p^{(N)}$ converges almost surely to the population minimizer p^{∞}. Within the IFR framework, this is the precise sense in which redundant observation drives objectivity: the collective barycenter loses sensitivity to the specific composition of the observer ensemble and becomes a stable geometric invariant. □